Mercury contents and isotope ratios from diverse depositional environments across the Triassic–Jurassic boundary

Yager, Joyce; West, A. Joshua; Thibodeau, Alyson; Corsetti, Frank; Rigo, Manuel; Berelson, William; Bottjer, David; Greene, Sarah; Ibarra, Yadira; Jadoul, Flavio; Ritterbush, Kathleen; Rollins, Nick; Rosas, Silvia; Di Stefano, Pietro; Sulca, Debbie; Todaro, Simona; Wynn, Peter; Zimmerman, Laura; Bergquist, Bridget

DOI:
10.1016/j.earscirev.2021.103775

Document Version
Peer reviewed version

Citation for published version (Harvard):
Yager, J, West, AJ, Thibodeau, A, Corsetti, F, Rigo, M, Berelson, W, Bottjer, D, Greene, S, Ibarra, Y, Jadoul, F, Ritterbush, K, Rollins, N, Rosas, S, Di Stefano, P, Sulca, D, Todaro, S, Wynn, P, Zimmerman, L & Bergquist, B 2021, 'Mercury contents and isotope ratios from diverse depositional environments across the Triassic–Jurassic boundary: towards a more robust mercury proxy for large igneous province magmatism', *Earth Science Reviews*, vol. 223, 103775. https://doi.org/10.1016/j.earscirev.2021.103775

Mercury contents and isotope ratios from diverse depositional environments across the Triassic–Jurassic Boundary: Towards a more robust mercury proxy for large igneous province magmatism

Joyce A. Yager[1^], A. Joshua West[1], Alyson M. Thibodeau[2], Frank A. Corsetti[1], Manuel Rigo[3], William M. Berelson[1*], David J. Bottjer[1*], Sarah E. Greene[4*], Yadira Ibarra[1,5*], Flavio Jadoul[6*], Kathleen A. Ritterbush[7*], Nick Rollins[1*], Silvia Rosas[8*], Pietro Di Stefano[9*], Debbie Sulca[1,10*], Simona Todaro[9*], Peter Wynn[1,11*], Laura Zimmermann[12*], Bridget A. Bergquist[12]

Keywords: end–Triassic extinction, mercury isotope, Triassic–Jurassic boundary, mercury

[1]*University of Southern California, Department of Earth Sciences*

[2]*Dickinson College, Department of Earth Sciences*

[3]*University of Padova, Department of Geosciences*

[4]*University of Birmingham, School of Geography, Earth and Environmental Sciences*

[5]*San Francisco State University, College of Science and Engineering*

[6]*Dipartimento di Scienze della Terra 'Ardito Desio', Universitá degli Studi di Milano*

[7] *University of Utah, Department of Geology and Geophysics*

[8]*Pontificia Universidad Católica del Perú, Geological Engineering Program*

[9]*Università degli Studi di Palermo, Department of earth and marine science (DiSTeM)*

[10]*University of California, Davis, Department of Environmental Toxicology*

[11]*University of Washington, Department of Earth and Space Sciences*

[12] *University of Toronto, Department of Earth Sciences*

*These authors are listed in alphabetical order

^Corresponding author: joyceannyager@gmail.com

ABSTRACT

Mercury is gaining prominence as a proxy for large igneous province (LIP) volcanism in the sedimentary record. Despite temporal overlap between some mass extinctions and LIPs, the precise timing of magmatism relative to major ecological and environmental change is difficult to untangle, especially in marine settings. Changes in the relative contents of Hg in sedimentary rocks through time, or 'Hg anomalies', can help resolve the timing of LIP activity and marine extinctions. However, major questions remain unanswered about the fidelity of Hg as a proxy for LIP magmatism. In particular, depositional (e.g., redox) and post-depositional (e.g., oxidative weathering) processes can affect Hg preservation in marine sediments. These factors pose challenges for confidently using Hg as a fingerprint of volcanism. Here, we use the Hg anomaly at the Triassic–Jurassic boundary to explore the opportunities and challenges associated with two approaches that may help build a more robust interpretation of the Hg proxy: (1) measurements from sediments from diverse depositional environments, including lithologies with low Hg and organic carbon content, and (2) the simultaneous use of Hg stable isotope ratios. We present and compare Hg records from five geographically disparate Upper Triassic–Lower Jurassic marine sections that represent nearshore, mid-shelf, deep-water, and carbonate platform settings. These sedimentary sections span the emplacement of the Central Atlantic magmatic province (CAMP) and the associated end–Triassic extinction (ETE). Total organic carbon contents, carbonate contents, and Hg contents and stable isotope compositions demonstrate the multiple ways in which different depositional environments impact how Hg anomalies are expressed in ancient marine sedimentary rocks. Although we observe an increase in Hg/TOC during the ETE in each

section, the pattern and duration of Hg enrichment differ notably between sections, and the timing is not always coincident with CAMP activity, illustrating how the depositional filter complicates the use of Hg/TOC ratios alone as a fingerprint of LIP magmatism. In addition, Hg isotope measurements support a volcanic origin for these Hg anomalies during the ETE, suggesting CAMP was the Hg source during the extinction interval. These data support the use of Hg isotopes to help distinguish Hg loading that results from LIP magmatism on a global scale and emphasize the importance of making Hg proxy measurements from diverse depositional environments.

1. INTRODUCTION

The prevalence of mass extinctions coincident with large igneous province (LIP) activity motivates a thorough understanding of the connections between magmatism and global environmental change (e.g., Bond and Wignall, 2014). Extinctions may be caused or enhanced by the cascade of effects following the release of volcanic gases (e.g., S, CO_2) in high quantities over geologically short periods of time. These gases perturb the Earth system, potentially causing ocean acidification, ocean anoxia, and warming (or cooling), all of which may be detrimental to metazoan life (e.g., Bond and Wignall, 2014). Similarities between mass extinction–LIP emplacement intervals and modern anthropogenic CO_2 emissions underscores their relevance today (e.g. Foster et al., 2018). However, correlation between terrestrial sections (where LIPs often occur) and marine sections (where many of the extinction records occur) is typically not straightforward, motivating further work to better understand the relationship between LIP emplacements

and related extinctions. Mercury preserved in sedimentary rocks may help link LIP magmatism with biotic and other environmental changes observed in the marine sedimentary record, because Hg can be measured in the same sedimentary records that preserve paleontological evidence (e.g., Grasby et al., 2016, 2019; Percival et al., 2015; Sanei et al., 2012; Scaife et al., 2017; Shen et al., 2019a, b; Thibodeau et al., 2016, amongst many other recent studies).

In the absence of anthropogenic perturbation, Hg is primarily introduced to the atmosphere, ocean, and sedimentary record through volcanic inputs (e.g., Fitzgerald et al. 2014). In the geologic record, periods of high volcanic activity and associated increased input to the Earth system may be reflected in sedimentary intervals with unusually high Hg enrichments, termed 'Hg anomalies' (Sanei et al., 2012). Since Hg is often associated with organic matter in sediments, recent literature has focused on identifying Hg anomalies based on ratios to total organic carbon (TOC; reviewed by Grasby et al., 2019). The ease of measuring Hg and TOC contents in sedimentary rocks has led to a rapid proliferation in the application of this proxy across Phanerozoic LIP and mass extinction events.

As its application has grown, so too has the understanding of the complexity of factors that can influence Hg contents and Hg/TOC ratios in sedimentary rocks. The reliability of Hg contents as a proxy for LIP volcanism is significantly impacted by its host phase, which is often organic matter but can also be clays or sulfur species (e.g., Shen et al 2019a,b). Redox conditions and diagenesis impact the formation and preservation of these host phases and are all at least partially controlled by depositional environment. Additionally, post-depositional fluid flow and weathering can redistribute Hg, altering primary contents (Charbonnier et al., 2020). These multiple confounding factors may erase

93 the record of volcanic loading or generate Hg enrichments unrelated to volcanism (Shen et
94 al., 2019a), raising fundamental questions about whether increases in Hg content and/or
95 Hg/TOC ratios in sedimentary sections can be used as a simple and reliable fingerprint of
96 secular changes in volcanism.

97 The recognition of complexities is a vital step in the development of robust
98 geochemical proxies for past environmental change; an important next step is to explore
99 approaches and techniques that may provide for reliable interpretations despite the inherent
100 complexity (Elderfield, 2011). In this study, we explore two of the many possible directions
101 that may help develop a more robust Hg proxy. First, we ask whether measurements from
102 rock types that are low in Hg and TOC may help to broaden the applicability of the proxy,
103 as different depositional environments may differ in their deposition of sulfides, clays, and
104 TOC, and indirectly Hg contents. Mercury measurements are scarce in organic-poor
105 lithologies, in part because they are more difficult to measure and in part because prior
106 work has established thresholds of TOC content below which Hg/TOC ratios are regarded
107 as unreliable; however, this seems likely to be a product of ill-suited TOC methods and
108 difficulty interpreting low TOC samples, and we address both here. Second, and in tandem,
109 we evaluate how Hg isotopes may add vital but widely under-utilized information for
110 fingerprinting volcanism in the sedimentary record. Understanding how Hg isotope ratios
111 in sedimentary rocks are affected by local and regional cycling and depositional
112 environments remains incomplete yet critical to extracting the most from the
113 complementary information that they offer.

114 We address these two major questions by focusing on the Triassic–Jurassic
115 boundary (TJB), which is associated with one of the major Phanerozoic mass extinctions

and one of the iconic Hg anomalies that has enabled linking of the end-Triassic extinction (ETE) with LIP activity associated with the Central Atlantic magmatic province, or (CAMP) (Percival et al., 2017; Thibodeau et al., 2016). To this end, we present new records of Hg content and isotopic compositions from diverse depositional settings across this time interval. In the sections that follow, we begin with a review of the Hg proxy and its complexities; we follow by introducing TJB sedimentary sections that are focus of our study before presenting new records and discussing the implications of our data for use of the Hg proxy.

2. BACKGROUND

2.1 Hg as a proxy for LIP magmatism in the sedimentary record

Volcanic emissions comprise ~75% of present-day natural Hg emissions, making them the primary natural source of Hg to surficial reservoirs on Earth (Pyle and Mather, 2003). Mercury has an approximately 1 year residence time in the atmosphere, which enables its global distribution and deposition (Schroeder and Munthe, 1998; Lindberg et al., 2002; Douglas et al., 2008). From the atmosphere, Hg deposits into terrestrial and marine environments where it can be cycled back to the atmosphere between terrestrial and marine environments, with ultimately a major sink in marine sediments. Today, Hg has a deep-ocean residence time of ca. 350 years, much shorter than the whole-ocean mixing time (ca. 1000 years), and the surface ocean has an even shorter residence time (Gill and Fitzgerald, 1988). As a result, periods of intense volcanism can increase the global atmospheric Hg load and leave a systematic imprint on marine and terrestrial systems.

Once emitted, volcanogenic Hg can enter the marine system via atmospheric deposition or terrestrial runoff, and in both cases Hg is thought to be transferred to marine sediments mostly complexed with organic compounds and other particles (e.g., Kongchum et al., 2011; Zhong et al., 2008). Thus, Hg contents in marine sediments are highly dependent on the local organic load and/or dilution by non-Hg-bearing detrital sediments (Grasby et al., 2013), and local effects may dominate the Hg signature in coastal marine sediments. Although Hg is often associated with organic matter, in modern and ancient sediments it can also be associated with sulfides (e.g., Huerta-Diaz and Morse, 1992; Shen et al., 2019a; Shen et al., 2020) or clays (e.g., Them et al., 2019), depending on the redox conditions during and immediately after deposition.

Due to the particle-reactive nature of Hg accumulation in sediments, Hg contents are typically normalized to a host phase in order to identify changes in input to the atmosphere-ocean system, such as that from volcanic loading. Given the predominant associated of Hg with organic matter, total organic carbon (TOC) contents are widely used for normalization to ensure that observations of high Hg contents are not simply a product of high sedimentary TOC deposition in sediments. Observations of increases in Hg/TOC in multiple stratigraphic sections are hypothesized to reflect globally increased magmatism, and can help to relate the timing of magmatism with environmental and biotic changes recorded in the same sections (e.g., Percival et al., 2017; Grasby et al.,2 019).

Previous studies applying the Hg proxy have focused on sedimentary rocks with significant TOC content, which can easily be analyzed via thermal combustion methods. Previous work (recently reviewed by Grasby et al (2019)) exclueded Hg/TOC ratios from samples with <0.2% TOC. This threshold is presumably a holdover from analytical

methods that are unable to resolve lower TOC (e.g., Rock-eval pyrolysis); subsequent studies have adopted this cutoff regardless of the TOC analysis method and its detection limit. Many methods, such as those that use elemental analyzers, are capable of quantifying low TOC contents and have been reported in other studies (e.g., Fujisaki et al., 2018; Galy et al., 2007, 2008; Hilton et al., 2010; Scheingross et al., 2021) Here, we use a method that can quantify low TOC samples and further describe its capabilities and limitations in the supplement. Quantifying Hg/TOC ratios in low-TOC samples could open possibilities of working in a wider range of lithologies across a wider range of depositional environments than those available when restricted to samples with 0.2 wt.% TOC. Records from diverse lithologies across the same period of time could help to avoid 'false positive' Hg anomalies related to depositional artifacts. However, the challenge with this approach is not just analytical; the meaning of Hg/TOC values in samples with very low TOC remains to be fully understood.

2.2 Hg isotopes and the volcanic Hg proxy

Mercury isotopes can help identify the source of Hg in sediments and/or the pathway of deposition (i.e., atmospheric versus runoff). In particular, isotopic information can potentially identify anomalously high Hg contents originating from LIP magmatism (Thibodeau and Bergquist, 2017; Bergquist 2017). Mercury has seven stable isotopes and undergoes both mass dependent fractionation (MDF) and mass independent fractionation (MIF). Mass dependent fractionation in Hg isotopes is typically reported using the $^{202}Hg/^{198}Hg$ ratio as $\delta^{202}Hg$ (where $\delta^{202}Hg$ (‰) = $[(^{202}Hg/^{198}Hg)_{sample}/(^{202}Hg/^{198}Hg)_{standard} - 1] \times 1000$). The NIST 3133 standard is widely used for Hg isotope measurement and is adopted here (Blum and Bergquist, 2007). Mass independent fractionation is measured as

184 the difference between another measured δ value (e.g., δ^{199}Hg) and the MDF predicted
185 using the measured δ^{202}Hg value and the kinetic MDF law; this difference is typically
186 reported as Δ^{199}Hg for odd isotope MIF.

187 Gaseous elemental Hg emitted from volcanoes enters the atmosphere with no
188 measurable MIF (Δ^{199}Hg = 0‰; Fig. 1a) and with negative to zero MDF (δ^{202}Hg = –2‰
189 to 0‰; e.g., Zambardi et al., 2009; Szponar et al., 2020; Si et al., 2020). After oxidation of
190 elemental Hg to more reactive and particle-reactive species, Hg can acquire odd MIF
191 mostly via photochemical reduction either in cloud droplets, surface waters, or on surfaces
192 in terrestrial settings (Thibodeau and Bergquist, 2017; Bergquist 2018). This results in
193 gaseous elemental Hg in the atmosphere having negative odd MIF compositions and
194 oxidized Hg species having positive odd MIF signatures (Blum et al., 2014). Because much
195 of the Hg accumulated in terrestrial soils is from uptake of gaseous elemental Hg by
196 vegetation (Zhou et al., 2021), terrestrial soils and surfaces typically preserve negative odd
197 MIF values (i.e., negative Δ^{199}Hg) and much more negative δ^{202}Hg or "negative MDF" in
198 biomass and soils due to the preferential uptake of the lighter Hg isotopes (Demers et al.,
199 2013). Nearshore sediments that acquire Hg through terrestrial runoff thus typically exhibit
200 negative MIF and more negative MDF Hg isotope values (Demers et al., 2013; Zheng et
201 al., 2016; Thibodeau and Bergquist, 2017; see Fig. 1a). In contrast, settings further from
202 the continent usually contain small odd-isotope excesses (i.e., positive Δ^{199}Hg and Δ^{201}Hg
203 values, or "positive MIF" and less negative δ^{202}Hg), which are from the deposition of
204 oxidized Hg species (Thibodeau and Bergquist, 2017; Bergquist and Blum, 2007; Sonke
205 2011).

206 Thibodeau et al. (2016) measured Hg isotopes in shallow marine sediments
207 spanning the Triassic–Jurassic boundary (TJB) and speculated that the absence of MIF
208 observed in these rocks during the end–Triassic extinction was due to increased volcanic
209 loading of Hg associated with the central Atlantic magmatic province (CAMP). Since then,
210 other studies have reported Hg isotope values associated with Hg anomalies during other
211 LIPs, including at the end–Permian (Grasby et al., 2017; Shen et al., 2019a,b; Wang et al.,
212 2018), during the Toarcian ocean anoxic event (Them et al., 2019), across the Ordovician–
213 Silurian boundary (Gong et al., 2017), and at the Cretaceous–Paleogene boundary (Sial et
214 al., 2016). Since volcanic Hg often initially exhibits negative MDF and MDF can be altered
215 by many other environmental processes, MDF is not as diagnostic as MIF in fingerprinting
216 magmatically sourced Hg. Here we focus our discussion on MIF signatures, which are
217 thought to be more useful for fingerprinting volcanic Hg.

218 **2.3 Complications in using the Hg proxy for LIP magmatism**

219 Although Hg contents and isotopes are a promising proxy in many respects, a
220 growing number of studies are revealing that multiple, complex processes may influence
221 the preservation and magnitude of Hg and Hg/TOC anomalies. Release of Hg during LIP
222 activity may be influenced by magmatic style as well as non-volcanic sources such as fires
223 on land or release of sedimentary Hg by magmatic intrusions and emplacement (Grasby et
224 al., 2017). Periods of LIP activity were also likely characterized by both intrusive and
225 extrusive magmatism, and by eruptions that ranged from the subaerial to the submarine. It
226 is unclear how these different styles of eruption would have affected the release and
227 deposition of Hg and the resulting signals recorded in sedimentary records. It is possible
228 that subaerial, explosive volcanism may have led to more Hg in globally distributed

depositional environments, while submarine and effusive volcanism may not have perturbed the global Hg cycle to the same extent (Percival et al., 2018).

Additional complexity in Hg records also results from depositional and diagenetic processes (Percival et al., 2018; Charbonnier et al., 2020), including local redox fluctuations (Shen et al., 2019a). Some apparent anomalies may be better explained by local redox variability than by volcanic emissions of Hg (Them et al., 2019; Shen et al., 2019a), and the known association between Hg and sulfur in many sedimentary rocks (Huerta-Diaz and Morse, 1992; Shen et al., 2020) and clays (Manceau et al., 2018; Shen et al., 2019a, b**)** raises questions about whether TOC normalization alone accounts for the key processes driving Hg enrichment or depletion in some environments (Sanei et al., 2012; Shen et al., 2019a; Shen et al., 2020).

Given the complexity of Hg contents and Hg/TOC ratios in marine sediments, Hg isotopes may offer key complementary information for fingerprinting LIP magmatism. Despite a large number of studies measuring Hg contents and Hg/TOC ratios in a range of depositional environments, there are few studies that utilize Hg isotopes to understand the origin of Hg anomalies across depositional settings. A systematic investigation of Hg isotopes in different depositional settings from the sedimentary record is important to further understand the role of LIP magmatism (among other processes) in driving changes in sedimentary Hg. Understanding such effects is particularly important because multiple records of Hg, Hg/TOC, and Hg isotopes from the same time period are necessary to demonstrate that perturbations to the Hg cycle are indeed global and not local (Percival et al., 2017). Understanding site-dependent effects associated with depositional environment may be critical to evaluating similarities and differences between sections. Here, we

explore how the depositional environment affects Hg contents and the Hg isotope signal across four different sections spanning the TJB, when a well-defined Hg anomaly has been previously identified and tied to LIP activity (Thibodeau et al., 2016; Percival et al., 2017).

2.4 The Triassic–Jurassic Transition: A testbed for the Hg proxy

The CAMP (Marzoli et al., 1999) was a subaerial magmatic province emplaced over approximately one million years during the Late Triassic and Early Jurassic (Davies et al., 2017; Blackburn et al., 2013; Knight et al., 2004). Intrusive activity began ca. 100 kyrs before the dominant extrusive activity (Davies et al., 2017). Emplacement was likely characterized by 3–4 main pulses (Blackburn et al., 2013) of durations somewhere between 1–100 kyrs (Schaller et al., 2012; Berner and Beerling, 2007).

The end–Triassic extinction (ETE; 201.56 Ma) coincided with CAMP activity (Marzoli et al., 2004; Schoene et al., 2010; Wotzlaw et al., 2014). The record of the ETE is largely preserved in marine sediments, in which direct evidence of CAMP activity at many localities is scarce. Thus, our understanding of the ETE and the TJB transition can be greatly enhanced by the successful application of the Hg proxy, if Hg provides a fingerprint of CAMP volcanism that can be related directly to the marine record of extinction across multiple stratigraphic sections (Percival et al., 2017; Thibodeau et al., 2016). However, records of Hg contents from this time are different at each section that has been measured to date. Mercury contents and Hg/TOC differ by orders of magnitude from section to section, relative increases (i.e., anomaly severity) in each section are different, and the relative timing of anomalies based on chemo- and biostratigraphy and the extinction record are not consistent, raising questions about how increases in Hg or

Hg/TOC can be directly interpreted as fingerprints of LIP volcanism (Kovács et al., 2020; Lindström et al., 2019; Percival et al., 2017; Ruhl et al., 2020; Thibodeau et al., 2016).

In this study, we target five sedimentary sections that span the TJB and represent a range of depositional environments, from shallow through deep marine (here, we use the term "deep marine" to refer settings that are still on the continental margin but well below storm wave base in basinal settings). We also consider a carbonate platform. We report Hg contents, Hg/TOC ratios, and Hg isotopes from these localities and explore how differences and similarities in their Hg records may be tied to depositional setting and associated sedimentary processes.

3. OVERVIEW OF LOCALITIES

We collected samples and measured Hg from five open marine sections (although we note some debate exists for St. Audrie's Bay) spanning the Triassic–Jurassic boundary from disparate paleogeographic locations (Fig. 1a) and from a range of depositional settings with variable expected influences on the Hg proxy (Fig. 1b). We deliberately chose depositional settings characterized by lithologies that have been widely used in applying the sedimentary Hg proxy (specifically, rocks with substantial TOC) as well as those that have been less well studied, including carbonate-dominated rocks with low TOC. In working with low-TOC carbonates, our goal was to explore both analytical and interpretive limits.

Most samples have a corresponding thin section for further lithologic comparison. Each locality has a well-characterized bio- and/or chemostratigraphic context; the position of the ETE and Triassic–Jurassic boundary are denoted in Figs. 2–7 and are based on

297 previous studies. We correlated each section and demarcated the end–Triassic extinction
298 based on the negative carbon isotope excursion seen in organic matter at each section (e.g.,
299 Yager et al., 2017; their fig. 2). There is currently a lively debate regarding the source of
300 the organic carbon isotope excursion (e.g., Lindström et al. 2012), the ability to correlate
301 it between ocean basins (Fox et al., 2020), and its relationship to the ETE extinction.
302 However, given the presence of the initial carbon isotope excursion in Peru (Yager et al.,
303 2017), Canada (Williford et al, 2007), Nevada (Guex et al., 2004; Ward et al., 2007), Japan
304 (Fujisaki et al., 2018), Argentina (Ruhl et al., 2020), and many European sections (e.g.,
305 Lindström et al. 2012; Fox et al. 2020) and that in each of those sections it coincides with
306 the onset of the mass extinction, we think using a biostratigraphic and C isotope-based
307 correlation is reasonable. In any case, we note that different possible correlations, such as
308 those suggested by Lindström et al. (2019) and Zaffani et al. (2018), will not change our
309 conclusions.

310 **3.1 New York Canyon, Nevada, USA**

311 The New York Canyon area of Nevada, USA includes a well-studied Panthalassic
312 record from the Triassic–Jurassic boundary (e.g., Taylor et al., 1983; Guex et al., 2004 and
313 references therein). The section is exposed on Ferguson Hill, which forms the northern
314 portion of Muller Canyon, is the auxiliary global stratigraphic section and point for the
315 period boundary (Bown et al., 2007; Morton and Hesselbo, 2008). The Gabbs Formation
316 and overlying Sunrise Formation comprise limestone, silty shale, and silty marl (Fig. 3),
317 with detailed biostratigraphy (the ammonite *Psiloceras spelae*; Guex et al., 2004)
318 indicating the Triassic–Jurassic boundary within the upper Gabbs Formation. Several
319 studies of the organic carbon (C) isotope signature ($\delta^{13}C_{org}$) at the Ferguson Hill section

320 (Bartolini et al., 2012; Guex et al., 2004; Ward et al., 2007; Corsetti et al., 2015) document
321 a negative excursion in $\delta^{13}C_{org}$ at the extinction horizon.

322 Upper Triassic rocks of the Gabbs Formation are interpreted to represent a robust
323 carbonate ramp (the Mount Hyatt Member), overlain by a finer-grained middle-shelf
324 deposit (the uppermost Muller Canyon Member). Lower Jurassic rocks first appear within
325 the Muller Canyon Member of the Gabbs Formation and persist into the increasingly thick
326 and resistant beds rich in limestone and chert, in the overlying Ferguson Hill Member of
327 the Sunrise Formation (Schoene et al., 2010), which are interpreted to represent a middle-
328 ramp setting on a distally-steepened bioclastic habitat (Ritterbush et al., 2014; Taylor et
329 al., 1983). We interpret the rocks in this section as indicative of a local upward-shallowing
330 trend, which began in the Late Triassic and continued into the Early Jurassic (Sinemurian).
331 The paucity of inorganic carbonate and other benthic bioclastic content throughout the
332 Muller Canyon Member has been attributed to either a global drop in carbonate saturation
333 (but see Greene et al., 2012) or to a loss of carbonate producers during the extinction
334 interval (Kiessling et al., 2007; Ritterbush et al., 2014). Overall, the New York Canyon
335 area represents deposition along the mid to inner shelf (Fig. 3) (Ritterbush et al., 2014).

336 **3.2 St. Audrie's Bay, UK**

337 The St. Audrie's Bay section has been well studied for over 100 years (e.g.,
338 Richardson, 1911, 1906, 1905). The ammonite *Psiloceras spelae*, which denotes the base
339 of the Jurassic (Guex et al., 2004, Guex et al., 2012), is absent in the section, so we rely on
340 the presence of the aforementioned negative CIE and subsequent positive shift in $\delta^{13}C$ (e.g.,
341 Yager et al., 2017; Lindstrom et al., 2012) to place the Triassic–Jurassic boundary at ~15
342 m in the St. Audrie's Bay section (similar to Hesselbo et al., 2004; we note the possibility

343 that this isotope excursion may also reflect a period of subaerial exposure as suggested by
344 Fox et al., 2020, but argue that this would not fundamentally change our correlation).

345 The section at St. Audrie's Bay includes dramatic changes in depth, TOC (wt.%),
346 and calcium carbonate content (wt.%). Hesselbo et al. (2004) provided a thorough
347 summary of the depositional changes seen at the section, which we briefly summarize here
348 (we followed the stratigraphy from Hesselbo et al., 2004, for our sampling and use their
349 stratigraphic column in Fig. 4). The lowermost ~2 m comprise the Williton Member of the
350 Blue Anchor Formation, which consists primarily of mudstone, has marine trace fossils
351 and bivalves, and is interpreted as shallow marine (Hesselbo et al., 2004; Mayall, 1981).
352 Meters ~2–12 comprise the Westbury Formation, which consists of mudstone and siltstone
353 with carbonate concretions and phosphatic conglomerate (Hesselbo et al., 2004;
354 Richardson, 1911, 1906). The Westbury Formation is characterized by relatively low TOC
355 (although note scale difference for TOC between Figs 3–6), and carbonate is typically in
356 diagenetic concretionary horizons. The Westbury Formation is generally interpreted as
357 deeper and further offshore compared to the Williton Member, but the uppermost Westbury
358 Formation documents a shallowing (Hesselbo et al., 2004). The Cotham Member of the
359 Lilstock Formation overlies the Westbury Formation, comprises mudstones and
360 limestones, and is interpreted as a shoreface equivalent to the Westbury Formation
361 (Hesselbo et al., 2004). The Cotham Member contains an erosional surface, desiccation
362 cracks, and ooids, representing a substantial shallowing relative to the rest of the section,
363 subaerial exposure, and potentially non-marine conditions (Hesselbo et al., 2004 and
364 references therein). The negative CIE occurs in the Cotham Member, and thus this interval
365 likely represents the ETE. Although not found at St. Audrie's Bay, sections nearby contain

366 stromatolites in association with the negative excursion (Ibarra et al., 2016), and their
367 widespread occurrence suggests the absence of fauna and further supports the interpretation
368 of this interval as representing the ETE. The Langport Member of the Lilstock Formation
369 comprises limestone and mudstone and is interpreted as fully marine but relatively shallow
370 based on wave-generated ripples (Hallam, 1960; Richardson, 1911; Swift, 1995). Above,
371 the Blue Lias Formation comprises organic-rich shale and limestones that are likely a
372 product of diagenetic mobilization of carbonate (Hallam, 1964). Burrowing intensity varies
373 substantially in the Blue Lias Formation, and carbonate-rich beds typically reflect less
374 organic-rich, oxygenated settings while the more organic rich facies are interpreted to
375 reflect an anoxic sediment water interface (Hesselbo et al., 2004). Fossils and pyrite are
376 common and suggest marine but potentially euxinic conditions in the water column or
377 sediment water interface (Hesselbo et al., 2004; Wignall, 2001).

378 In summary, the shallowest portion of the St. Audrie's Bay section is during the
379 ETE, while the remainder of the exposed Rhaetian and Hettangian are relatively deeper but
380 with very different TOC and carbonate contents, likely due to differences in conditions at
381 the sediment water interface and during early diagenesis.

382 **3.3 Lombardy Basin, Southern Alps, Italy**

383 The Lombardy Basin (Southern Alps, Italy) is a rift-related basin developed during
384 the Mesozoic. The Upper Triassic to Lower Jurassic succession (upper Norian to
385 Sinemurian) comprises a mixed marly-carbonate to carbonate succession deposited on the
386 western margin of Tethys (e.g., Jadoul et al., 2012; Zaffani et al., 2018). The lower portion
387 of the Calcari di Zu Formation (i.e., Zu Limestones) is upper Norian–Rhaetian and contains
388 common bivalves and foraminifera. Cycles of dark marls transition upwards into limestone

389 (Zu-1 Member; Fig. 5; Fig S1). These beds successively develop into centimeter-scale
390 carbonate beds interlayered with very thin, shale-rich intercalations (Zu-2 Member; Fig. 5;
391 Fig S1) (Galli et al., 2007; Zaffani et al., 2018). These cyclic packages comprise
392 bioturbated and fossiliferous wackestones and packstones, with patch reefs, sponges, and
393 foraminifers overlain by cyclic packages consisting of thick marl and micritic fossil-rich
394 limestones (Zu-3 Member; Fig. 5; Fig S1) containing benthic foraminifers, bivalves,
395 calcareous sponges, and corals (Galli et al., 2007; Zaffani et al., 2018). The Malanotte
396 Formation unconformably overlies the Calcari di Zu Formation and represents the
397 outermost and deepest portion of the carbonate ramp environment. It consists of thin-
398 bedded micritic limestones and mudstones, with rare bioclasts at the base and abundant
399 reworked ooids in the upper part as it grades into the Albenza Formation (Galli et al., 2007).
400 The Albenza Formation represents a regional progradation of the Hettangian carbonate
401 platform, characterized by amalgamated beds of oolitic and bio-intraclastic grainstones,
402 which are locally dolomitized (Galli et al., 2007). This carbonate platform slowly drowned
403 during the Hettangian into an open subtidal shelf environment, represented by the Sedrina
404 Formation, which comprises mudstones–wackestones and thin marl intercalations, with
405 common black chert nodules, sponge spicules, brachiopods, pelagic bivalves, and rare
406 ammonites (Bersezio et al., 1997). The Sedrina Formation grades into the Sinemurian–
407 Pliensbachian Calcare di Moltrasio Formation (i.e., Moltrasio Limestones; Fig. 5; Fig S1),
408 which is dominated by gray marl limestones and black cherts with slumps and calcarenitic
409 beds, representing a fully pelagic environment (Bersezio et al., 1997).

410 We sampled the Lombardy Basin succession at four sections that would allow us
411 to sample the mid-Rhaetian (Zu Limestone) through the mid-Hettangian (Moltrasio

412 Formation) and into the Sinemurian; no single section covers the entire Rhaetian–
413 Hettangian. We sampled the Zu Limestone at the Brumano Section, which exposes ~200
414 m of stratigraphy that extends from the upper Norian (Zu-1 Member) to the mid-Rhaetian
415 (middle of Zu-3) (Zaffani et al., 2018). We sampled ~120 m of this section from Zu-2 (just
416 above the Norian–Rhaetian boundary) to the top of the Zu-3a sub-member at the top of the
417 section (Muttoni et al., 2010). We sampled the upper Zu Formation (sub-members 3b and
418 3c) up to the base of the Malanotte Formation at the Italcementi Quarry. The Triassic–
419 Jurassic boundary is placed within the Zu-3c sub-member (Zaffani et al., 2018). There are
420 multiple sections at the Italcementi Quarry, and we sampled from the inactive quarry (~100
421 m total stratigraphy), corresponding to the same sites used by Zaffani et al. (2018). Only
422 the very base of the Malanotte Formation is exposed at the Italcimenti Quarry; we sampled
423 the remainder of this formation along the Valcava-Torre di Busi road (the ~30 m Malanotte
424 section from Galli et al., 2005). Finally, we sampled the upper portion of the Malanotte
425 Formation extending through the Albenza and Sedrina formations into the Moltrasio
426 Formation at Val Adrara (corresponding to the well-studied section described and studied
427 by Bachan et al., 2012; Galli et al., 2007; Van de Schootbrugge et al., 2008; Jost et al. 2017
428 and others). We sampled the lower ~350 m of the Val Adrara section. To generate a
429 composite stratigraphic section for the Lombardy Basin samples used in this study, we
430 correlated between sections based on formation boundaries, biostratigraphy, and
431 chemostratigraphy ($\delta^{13}C$); a detailed correlation between these sections is available in the
432 supplementary information.

433 **3.4 Panormide platform, Sicily, Italy**

434 The Triassic and Lower Jurassic shallow water carbonates from Sicily are
435 dolostones and limestones that crop out in the Sicilian Maghrebian chain and in the
436 subsurface of the foreland areas of the Hyblean plateau and Sicily Channel (Antonelli et
437 al., 1988; Patacca et al., 1979). These rocks were deposited in a wide carbonate embayment
438 that was flanked by deep water basins in the southwestern branch of Tethys (Di Stefano et
439 al., 2015; Zarcone et al., 2010). During the Late Triassic, the carbonate platform edge was
440 a Dachstein-type reef complex dominated by hypercalcified coralline sponges that are now
441 well exposed in the Palermo and Madonie Mountains and in central-southern Sicily (Di
442 Stefano et al., 2015). The reef complex transitioned to an escarpment and to a deep water
443 basin, while the back reef zone was characterized by extensive lagoons. Westward, a
444 transition to evaporite facies (sabkha-type) characterized the innermost zone of the
445 carbonate platform (Lo Cicero, 1986). The shallow water carbonate sedimentation lasted
446 until the late Sinemurian–Pliensbachian, when the platform experienced a drowning.
447 In Sicily, the Triassic–Jurassic transition in peritidal settings has been documented
448 in a few areas from the Hyblean foreland and in the Sciacca area (Cacciatore et al., 2006;
449 Patacca et al., 1979). More recently, a well exposed and continuous peritidal succession
450 ~430 m thick, encompassing the Triassic–Jurassic boundary, was described in detail in
451 Northwestern Sicily (Mt Sparagio, San Vito Lo Capo Peninsula; Todaro et al., 2018, 2017).
452 In this section, the peritidal limestones are organized in shallowing upward cycles (1.5 m
453 thick on average) characterized by subtidal, intertidal and supratidal facies (D'Argenio,
454 1974; Strasser, 1991). Based on the fossil content in the subtidal facies, the Mt Sparagio
455 section is divided into three informal units: unit A records the common occurrence of very
456 large megalodontid shells (up to 30 cm in size), coral patch reefs, and benthic foraminifers

such as *Triasina hantkeni* Majzon, *Auloconus permodiscoides* (Oberhauser), *Aulotortus sinuosus* (Weynschenk), *Aulotuortus* sp., *Glomospirella* sp., *Trochammina* sp., *Frondicularia* sp., *Nodosaria* sp. (Todaro et al., 2017). Some horizons contain calcareous algae, classified as *Cayeuxia* sp. and *Orthonella* sp. The presence of *Triasina hantkeni* indicate this unit is Rhaetian in age. Unit B shows the same benthic foraminifera assemblage as unit A, with differences in the macro benthic community, as corals disappear and a change in the size of megalodontids is observed (Todaro et al., 2017, He et al., 2020). The upper boundary of unit B is identified based on the last occurrence of the Rhaetian benthic community and by the presence of an oolitic horizon. Above, there is a ~10 m thick fossil-poor interval that contains only small calcispherae. Unit C consists of oligotypic facies characterized by a bloom of the alga *Thaumatoporella parvovesiculifera* in association with *Aeolisaccus* sp, and, higher up, by *Siphovalvulina* sp. This fossil assemblage is considered typical of the Hettangian–Sinemurian interval (Barattolo and Romano, 2005, Boudagher-Fadel and Bosence, 2007).

3.5 Levanto, Peru

The Levanto section in northern Peru spans the Upper Triassic and Lower Jurassic; the ~105 m section is continuous for ca. four million years. The entirety of the outcrop consists of the Aramachay Formation, which, at this location, comprises carbonate-rich mudstones with abundant intercalated ash beds (Fig. 6). U–Pb dating of zircons of the ash beds and ammonite biostratigraphy (Guex et al., 2012; Schaltegger et al., 2008; Schoene et al., 2010; Wotzlaw et al., 2014) have constrained the durations of the Rhaetian and Hettangian, and the chronology provides a valuable biostratigrahic and temporal framework for geochemical work at the section. The section is well below storm wave base

and is characterized by little bioturbation, which we interpret as indicative of anoxic conditions at the sediment water interface during deposition, persisting from the Rhaetian through Hettangian. Previous work on carbon isotopes, TOC, and carbonate content (Yager et al., 2017) record a typical Triassic–Jurassic boundary carbon isotope profile. Unlike many Tethyan sections, Levanto is characterized by lower TOC during the Hettangian relative to the Rhaetian. Carbonate content remains relatively high (~60%) through much of the section but is variable, particularly at the top of the section, where carbonate is concentrated in thick beds.

The first ~57 meters of the continuous section is characterized by alternating thin and thick-bedded intervals, though this alternation has little influence on sedimentary structures or lithology as observed in thin sections (Yager et al., 2017). At approximately 57 m, this alternation changes to meter-scale differences, and eventually (~80 m) grades into concretionary bedding and finally into meter-scale concretions (~85). Thin sections contain carbonate-replaced radiolarians, rare foraminifera, sponge spicules, and low contents of coarse detrital material (<5%). Pyrite is absent in the section, in stark contrast to St. Audrie's Bay. In summary, the Levanto section records a relatively static depositional environment spanning ca. four million years and has robust geochronological and biostratigraphic constraints.

4. MATERIALS AND METHODS

4.1 Sample processing

Samples were collected from outcrop and then cut to remove weathered material, veins, and modern marine-derived debris (specifically from St. Audrie's Bay samples).

503 Portions of samples were crushed in a jaw crusher and pulverized either in a stainless steel
504 disk crusher (New York Canyon samples) at the University of Southern California, Los
505 Angeles, CA USA (USC), in a tungsten carbide ball mill at USC (St. Audrie's Bay
506 samples), or at Actlabs in Ontario, Canada (Levanto and Lombardy Basin samples). Long
507 term blank testing indicated none of the powdering processes resulted in Hg contamination.

508 **4.2 Hg contents**

509 For the St. Audrie's Bay, New York Canyon, and Levanto samples, total Hg was
510 measured using a Hydra IIc at The University of Toronto (Toronto, Canada), using similar
511 methods to those from Thibodeau et al. (2016). In the Hydra IIc, weighed sub-samples of
512 powdered rocks were combusted under O_2 flow at 350 ml/min, heated in a drying step to
513 300ºC for 40 s, then decomposed for 300 s at 800ºC. Following combustion, evolved gases
514 were carried through a heated (600ºC) catalyst tube to remove possible interferences (e.g.,
515 halogen compounds, sulfur oxides, nitrous oxides) and Hg was captured on a gold trap
516 while combustion gases were removed from the detection cell. The gold trap was heated
517 for 30 s at 600ºC to release Hg, which was then carried to the detection cell where
518 absorbance from a mercury lamp is measured at 253.7 nm. For this study, instrumental
519 response was calibrated using the NIST 3133 Hg standard in a 0.25% L-cysteine solution.
520 Blank absorbance was <2% of typical sample signals and always <4%. NIST 3133 was
521 periodically combusted and analyzed alongside samples to determine precision, with
522 results within 5% of the nominal values. Samples measured more than once are reported
523 as averages, which typically have reproducibility better than 10%. External standards NIST
524 SRM 1944 and 1646a were combusted alongside samples to check measurement accuracy.

Errors on Hg content measurements are estimated to be 10% (2sd) based on reproducibility of samples and external standards.

Lombardy Basin and preliminary Panormide Domain samples were analyzed for total Hg concentrations using an MA-3000 Direct Mercury Analyzer (Nippon Instruments Corporation, Tokyo, Japan) thermal decomposition analyzer at USC. Similar to the Hydra IIc, the MA-3000 combusts powdered samples, uses a catalyst to remove interferences, traps Hg on a gold trap, and measures the amount of Hg after release from the trap by absorbance at 253.7 nm. The MA-3000 allows for combusting multiple aliquots of a single sample in order to accumulate enough Hg for analysis after release from the gold trap. This approach is well suited to samples with low Hg contents, such as the rocks from the Lombardy Basin. Total sample masses of up to 5 g were analyzed by combusting up to 20 ~250 mg sub-samples. Even with this approach, several samples contained too little Hg to obtain robust results, because the detection limit of 1.5 ng could not be reached with a reasonable number of combustions for some samples. Samples from the Lombardy basin that were below the detection limit are noted in the supplementary dataset. No samples from the Panormide domain in Sicily were above the detection limit, and results from this section are not reported here. We consider these to represent the analytical limit of Hg content measurement via the widely-used thermal decomposition method, though other analytical methods might allow Hg quantification in such rocks.

4.3 Hg isotope measurements

Mercury isotope measurements followed the analytical methods from Thibodeau et al. (2016). Briefly, Hg was extracted and purified from samples using the Hydra IIc without the gold trap (with a longer decomposition time than that used for Hg concentration

548 measurements). Mercury was trapped by directly sparging the gas outflow with elemental
549 Hg into ~10% H_2SO_4 (v/v) and ~1% $KMnO_4$ (w/w), which oxidized the Hg0 gas to HgII.
550 To ensure removal of residual Hg in the furnace, after each sample combustion, 50 µL of
551 Milli-Q was combusted and lines were heated with a heat gun to transfer any residual Hg
552 to the trap. NIST 3133 and 1646a were combusted and trapped as procedural standards and
553 blanks.

554 Procedural blanks were <0.02 ng/g, which is <1–2% of the sample Hg. Mercury
555 recovery was checked by neutralizing an aliquot of each solution with NH_2OH-HCl
556 immediately after vapor trapping and measuring its concentration using a Tekran 2600 cold
557 vapor atomic fluorescence spectrometer (Tekran instruments, Toronto, Canada). The ~10%
558 variation in sample recoveries reflects the uncertainty in concentration analyses and sample
559 heterogeneity. Mercury isotope analyses were conducted with a cold vapor multi–collector
560 inductively coupled mass spectrometer (Neptune Plus MC–ICP–MS, Thermo-Finnigan,
561 San Jose, CA, USA) at the University of Toronto. Sample solutions were neutralized with
562 NH_2OH-HCl and diluted to 1–2 ng/g with a matrix matched solution. Mercury was
563 introduced to the plasma as Hg0 after $SnCl_2$ reduction and Hg0 vapor separation on a gas–
564 liquid separator. A thallium internal standard and standard-sample bracketing with NIST
565 3133 were used to correct for instrumental mass bias, and an in-house Hg standard (J.T.
566 Baker Chemicals) was measured multiple times in each analytical session to determine
567 external reproducibility of the method. Signal concentrations and intensities of all
568 bracketing standards and samples matched within 10%. Isobaric interference from ^{204}Pb
569 was monitored using ^{206}Pb, but was always negligible (correction never altered the
570 calculated $\delta^{204}Hg$). On-peak blank corrections were made on all Hg and Pb masses.

All samples and procedural standards were measured at least twice, and sample isotope values are reported as the mean of duplicate or triplicate measurements (Tables S2 and S3). Average values for procedural standards are reported and are consistent with previous values for these standards (Thibodeau et al., 2016). Sample errors are reported as either the 2σ (standard error mean) of sample replicates or the 2σ (standard deviation) external reproducibility of the in-house J.T. Baker Hg standard, whichever is larger.

4.4 TOC and TIC

TOC: For samples from Levanto (Yager et al., 2017), St. Audrie's Bay, and New York Canyon, sub-samples of powders (~1 g) were treated with 1M HCl at 70°C for four hours to remove carbonate from the samples. Samples from the Italian sections (Brumano, Valcava Torre di Busi, and Italcementi) were treated the same way, but with 1 hr decarbonation times; our tests of decarbonation times indicate 1 hr heat treatments yield the same results for $\delta^{13}C$ and TOC as up to 8 hr decarbonation times (unpublished data). The samples then settled for 24 hours, the supernatant was decanted, and the decarbonated powder was rinsed three times with repetitive settling and decanting before being dried overnight at 50°C (after Galy et al., 2007). For dolomite-containing Val Adrara samples, this decarbonation procedure failed to fully remove carbonate, a problem identified by many unrealistically high $\delta^{13}C$ values for organic carbon (e.g., greater than –5‰). Additional sub-samples were treated with 3M HCl, agitated before heating (to expose all sample to acid), and then heated at 70°C for 1 hour to ensure complete carbonate removal. Acidified samples from Val Adrara were then centrifuged (2,000 RPM in an 8 inch diameter centrifuge) for 2 minutes in lieu of letting samples settle. Reported results for Italian samples are from this decarbonation procedure. We tested samples from New York

Canyon using both methods, and results were within the analytical uncertainty for both TOC and $\delta^{13}C_{org}$ measurements, supporting either method as a viable means of TOC and $\delta^{13}C_{org}$ measurement.

For all samples, TOC (wt.%) was determined on decarbonated powder using Picarro cavity ring down spectroscopy (CRDS; G2131-I; Santa Clara, CA, USA) coupled to a Picarro Liaison (A0301) and a Costech Elemental Combustion System (EA 4010, Valencia, CA, USA). Picarro measurements of CO_2 concentrations were calibrated to determine the percent of organic carbon in samples using the USGS 40 standard (L-glutamic acid) weighed at five different sample masses and run at the beginning and end of each set of ~15 samples. Determination of the reported sample TOC took into account the amount of carbonate lost during decarbonation (see further detail in supplemental information and Fig. S2). Uncertainty was determined by replicate analysis of samples and standards (typically ~2 replicates per sample; see Supplementary Table 1). Standard deviation of replicates for measured %TOC was ± 0.08 on average, or approximately ±3% of the measured value (1σ standard deviation). Because of potential errors introduced by small amounts of sample loss during liquid decarbonation, including via solubilization of organics (Galy et al., 2007), our conservative estimate of uncertainty is ±10% of the measured value for reported TOC. We elaborate further on our methods for TOC measurement in the supplement. Importantly, our methods do not have the same 0.2% TOC detection limit reported in many previous studies (typically measured via Rock-eval) and reviewed by Grasby et al. (2019), since we are able to calibrate the amount of organic carbon in our samples well within a standard curve (see supplemental information).

TIC: Depending on the sample's carbonate content, 3–200 mg of sample was weighed into 10 mL glass Exetainer vials with rubber septa caps. Vials were evacuated and acidified with 1 mL 30% H_3PO_4. Samples and standards were heated for 80 minutes in a water bath at 70°C to ensure that C associated with all carbonate phases was released as CO_2. Samples were then run on a Picarro CRDS coupled to an Automate preparation device, which sparges the solution with N_2 gas to drive CO_2 into the analyzer. In-house carbonate standards Optical calcite (OPT) and AR15 were run at different masses to calibrate total inorganic carbon (TIC). Errors were calculated by replicate analyses of samples and standards. Average error (1σ) for TIC measurements was ±0.04, or <1% of the measured value. Our reported carbonate contents (wt.%) were calculated from measured TIC, assuming all inorganic carbon in our samples is $CaCO_3$. No dolomite or other carbonate phases were observed in thin sections of the NYC, SAB, and Levanto samples. Dolomite is present in the Lombardy Basin samples, potentially introducing some uncertainty into carbonate content values for this section. These independent TIC analyses also allow for some constraint on the mass loss during decarbonation, which assist in understanding potential error introduced to TOC measurements (see supplemental information).

5. RESULTS

We report Hg contents, TOC contents, carbonate contents, and Hg isotope compositions in the supplemental data set. We analyzed 193 samples for Hg contents and 18 samples for Hg isotopes from the Levanto section, 80 samples for Hg contents and 13 for Hg isotopes from St. Audrie's Bay, and 81 samples for Hg contents from New York Canyon, complementing the previously published 35 content and 35 isotope measurements

639 from Thibodeau et al. (2016). The New York Canyon samples in this study are all
640 stratigraphically above those previously published in Thibodeau et al. (2016). From the
641 Lombardy Basin, we analyzed Hg contents in 24 samples from the Brumano section (11
642 yielding Hg above the detection limit), 57 from the Italcementi section (25 above the
643 detection limit), 21 from Valcava Torre de Busi (18 above the detection limit), and 29 from
644 Val Adrara (19 above the detection limit).

645 In Figs 3–6 we plot total Hg, TOC contents, Hg/TOC, δ^{202}Hg, and Δ^{199}Hg for each
646 section with stratigraphy. In each figure, 'pre' denotes the pre-extinction interval (i.e., the
647 available Rhaetian stratigraphy until the onset of the negative C isotope excursion), ETE
648 is denoted (i.e., from the onset of the negative CIE to the TJB), and 'post' denotes post-
649 extinction (i.e., Hettangian and above, where available). Figure S3 contains selected cross
650 plots of carbonate content, Hg, Hg/TOC, and TOC, with data separated by relative time
651 intervals (pre-ETE, ETE, and post-ETE).

652 **5.1 New York Canyon**

653 In Fig. 3 and Fig. S3a–c we report data from Thibodeau et al. (2017) and additional
654 data from this study. Prior to the ETE, samples have average Hg contents of ~12 ± 4 ppb
655 (n = 4; 1 s.d.). This value rises to ~50 ± 21 ppb (n = 14, 1 s.d.) during the ETE, and then
656 decreases to 11 ± 10 ppb (n = 100, 1 s.d.) during the Early Jurassic. Ratios of Hg/TOC have
657 average values of 48 ± 15 ppb/wt.% (n = 4; 1 s.d.) during the pre-extinction interval, rise
658 to an average of 244 ± 139 ppb/wt.% (n = 14; 1 s.d.) during the ETE, and decrease to an
659 average value of 92 ± 48 ppb/wt.% (n = 100; 1 s.d.) during the post-extinction interval.
660 Mercury isotope were originally reported and discussed in Thibodeau et al. (2017). The
661 δ^{202}Hg values during the Rhaetian and early Hettangian are between ~0‰ and –1.5‰,

becoming progressively more negative upsection; Δ^{199}Hg values are near zero during the ETE and in the early Hettangian, but deviate from zero (in both negative and positive directions) during the Hettangian. The New York Canyon section is truncated in the Rhaetian, so it was not possible to measure additional samples from before the extinction from this studied section. Mercury and TOC contents are not correlated during the ETE but are correlated ($r^2 = 0.50$) in the Hettangian samples (Fig. S3b).

5.2 St. Audrie's Bay

Figures 4 and S3d–f report data from St. Audrie's Bay. During the Rhaetian, average Hg contents are ~29 ± 15 ppb (n = 38, 1 s.d.), during the ETE (correlated using the negative CIE in organic C isotopes) average Hg contents are 19 ± 15 ppb (n = 13; 1 s.d.), and during the Early Jurassic Hg contents are 42 ± 29 ppb (n = 29; 1 s.d.). Ratios of Hg/TOC during the pre-extinction interval are on average 43 ± 27 ppb/wt.%TOC (n = 38; 1 s.d.), during the ETE are 102 ± 77 ppb/wt.% (n = 13; 1 s.d.), and during the Early Jurassic are 18 ± 20 ppb/wt.%TOC (n = 29; 1 s.d.). Ratios of Hg/TOC rise to ~150 ppb/wt.% coincident with the onset of the negative C isotope excursion (meter ~12) and then decrease to an average of ~20 ppb/wt.% during the Hettangian. Mercury and TOC are correlated, particularly during the ETE ($r^2 = 0.51$) and the Hettangian ($r^2 = 0.90$; Fig S3e). Percival et al. (2017) also reported Hg data from St. Audrie's Bay, which are plotted in Fig. 4; their TOC data are from Hesselbo et al. (2002). Mercury contents from Percival et al (2017) match well with our data, and TOC data are similar in the two studies, but the interval during the negative carbon isotope excursion differs slightly, resulting in a difference in Hg/TOC ratios. This discrepancy could be due to heterogeneity in the section during

684 sampling or TOC methodological differences; the implications for this difference are
685 discussed in the figure caption.

686 Values of δ^{202}Hg at St. Audrie's Bay are similar throughout the measured section
687 and range between –1.50‰ and –0.50‰; Δ^{199}Hg values are negative during the Rhaetian
688 (–0.20‰ to –0.40‰), increase to about –0.10‰ during the ETE, and decrease again during
689 the Hettangian (–0.20‰ to –0.40‰).

690 **5.3 Lombardy Basin**

691 The Lombardy Basin results are separated into the four respective sections (Fig.
692 S1) and are reported in a composite section in Fig. 5. Considered together, the Lombardy
693 sections exhibit low Hg contents (all <15 ppb, and contents greater than ~6 ppb found only
694 in the Brumano section) and low TOC. Many samples contain so little Hg that the 1 ng
695 detection limit would have required an estimated 10–20 separate combustions, implying a
696 content well below 1 ppb (as noted above, we did not analyze samples with such little Hg).
697 Marly samples contain slightly more Hg and sometimes elevated TOC.

698 At the Brumano section, samples have an average Hg content of 7 ± 4 ppm (n = 11,
699 1s.d.), TOC average of 0.2 ± 0.1% (n = 26; 1 s.d.), and Hg/TOC average of 25 ± 7 wt.% (n
700 = 10; 1 s.d.). The Brumano section, which is the deepest of the composite Italian sections,
701 deepens upwards, with less carbonate in samples from further up-section. Many carbonate-
702 rich samples lower in the section were below the detection limit for Hg measurements.
703 Overall, the Brumano section Hg contents are low (below the detection limit to ~3 ppb) in
704 resistant, carbonate-rich beds and higher (between ~5 and 14 ppb) in marly, mudstone beds.

705 Samples from the Italcementi quarry section (Fig. S1) have average Hg contents of
706 4 ± 3 ppb (n = 25, 1 s.d.; not including 32 samples below detection limit), TOC contents

of 0.1 ± 0.04 wt.% (n = 22, 1 s.d.) and Hg/TOC ratios of 44 ± 26 (n = 22; 1 s.d.). The two high (>50) Hg samples ITZ62 and ITZ64 are from marly beds. Carbonate-rich beds exhibit somewhat lower Hg contents.

The Valcava Torre dei Busi section (Fig. S1) has average Hg contents of ~2 ± 1.5 ppb (n = 18; 1 s.d.), TOC contents of 0.08 ± 0.16 wt.% (n = 27; 1 s.d.) and Hg/TOC values of 44 ± 25 ppb/wt.% (n = 16; 1 s.d.).

The Val Adrara section (Fig. S1) contains average Hg contents of 2.7 ± 1.4 ppb (n = 19; 1 s.d.), TOC concentrations of 0.03 ± 0.03 wt.% (n = 15; 1 s.d.) and Hg/TOC of 140 ± 119 ppb/wt.% (n = 15; 1 s.d.). Although the highest Hg/TOC values are found above the Triassic–Jurassic boundary from the Hettangian portion of the Val Adrara section, a less pronounced rise in Hg/TOC is synchronous with the TJ boundary.

5.4 Levanto

In Figs 6 and S3g–i we report data from the Levanto section. Mercury contents are on average 33 ± 14 ppb during the Rhaetian pre-extinction interval, (n = 84; 1 s.d.), 37 ± 24 ppb (n = 14; 1 s.d.) during the negative CIE and ETE Hg concentrations, and 36 ± 19 ppb following the ETE during the Hettangian (n = 96; 1 s.d.). Hg/TOC during the pre-extinction interval is 24 ± 25 ppb/wt.% (n = 84; 1 s.d.), during the ETE is 30 ± 29 ppb/wt.% (n = 14; 1 s.d.), and following the ETE is 64 ± 36 ppb/wt.% (n = 96; 1 s.d.). There is an increase in Hg/TOC at ~57 meters, coincident with the negative CIE in organic carbon isotopes (Yager et al., 2017). Mercury and Hg/TOC are negatively correlated with carbonate (Fig S3h–i) during the ETE and Hettangian. Correlations between Hg and TOC are weaker than for the St. Audrie's Bay and New York Canyon sections (Fig. S3g–i); elevated Hg/TOC is expressed during the ETE and into the Hettangian. Values of δ^{202}Hg

are between about –1.30‰ and –0.30‰ for the measured section, with a possible excursion from –0.3‰ to –1.5‰ during the late Rhaetian and ETE; Δ^{199}Hg is slightly positive during the Rhaetian (~0.1‰) and near zero without discernable MIF during the ETE and Hettangian (±0.05‰).

In the Rhaetian portion of the Levanto section, there is no discernible lithologic control on Hg contents based on outcrop or thin section observations (i.e., neither high nor low Hg contents appear to be related to specific lithologic composition). In contrast, during the Hettangian, alternations in thick and thin bedded strata appear to impact Hg contents and Hg/TOC. Samples high in Hg are compacted and contain less carbonate and slightly higher TOC, while samples that are uncompacted and high in CARB contain less Hg and lower Hg/TOC (Fig. S4). At ~57 m, carbonate content variability increases and samples with lower carbonate contents are associated with higher Hg concentrations (Fig. S5). We note proximity of samples to ash beds did not have any discernible effect on Hg contents, and in fact the Rhaetian portion of the section includes more conspicuous ash beds than the Hettangian, indicating ash bed presence does not control Hg contents in these samples.

5.5 Consistent observations between sections

Using organic C isotopes as a correlation tool, at all four sections Hg/TOC rises during the negative CIE and, by inference, during the contemporaneous ETE. At New York Canyon and St. Audrie's Bay, Hg/TOC decreases during the Early Jurassic after its peak associated with the CIE and ETE (Fig. 7). In contrast, at Levanto, Hg/TOC increases during the negative CIE and ETE and then increases further in the early Jurassic, remaining elevated for the remainder of the section (Fig. 7). In the Lombardy Basin, Hg/TOC is briefly elevated during the pre-ETE interval, decreases and then increases again during the

753 ETE and negative isotope excursion, and then rises to the highest observed values during
754 the early Hettangian (although these very high values from the Val Adrara section are
755 associated with very low TOC). Thus, St. Audrie's Bay and New York Canyon both exhibit
756 relatively well-defined Hg anomalies, while those at Levanto and in the Lombardy Basin
757 appear more protracted and less clearly defined. Levanto and Lombardy also share
758 somewhat enigmatic brief spikes in Hg/TOC in the late Rhaetian, prior to the ETE and C
759 isotope excursion.

760 At St. Audrie's Bay, New York Canyon, and Levanto, each section also exhibits
761 negligible or low MIF (near zero Δ^{199}Hg) during the ETE. New York Canyon and Levanto
762 record a slightly negative shift in δ^{202}Hg during the Late Rhaetian and ETE, while low
763 sampling resolution in Hg isotopes at St. Audrie's Bay may obscure any similar trend at
764 this site. We were not able to measure Hg isotopes from the Lombardy sections.

765

766 **6. DISCUSSION**

767 All four sections contain elevated Hg/TOC during the ETE and negative CIE, when
768 compared to pre-extinction values. During the same interval, MIF of Hg isotopes (Δ^{199}Hg)
769 is near zero or shifts towards zero, suggesting an increase in Hg deposition derived from
770 subaerial volcanism associated with CAMP activity during the ETE. Below, we detail the
771 implications of elevated Hg/TOC and low MIF and discuss the caveats from our study and
772 next steps for using and understanding the Hg proxy.

773

774 **6.1 Mercury isotopes support a magmatically derived Hg signal at the ETE**

775 At New York Canyon, Levanto, and St. Audrie's Bay, elevated Hg/TOC values
776 during the ETE coincide with Hg isotope signals that exhibit negligible MIF (Fig. 7),
777 consistent with a large increase in volcanic Hg that overwhelmed the surface reservoirs in
778 a way that resulted in minimal MIF producing photoreduction prior to deposition
779 (Thibodeau and Bergquist, 2017). Outside of the extinction interval, Hg isotopes are
780 consistent with normal Hg cycling through surface reservoirs, acquiring positive and
781 negative MIF (e.g., Bergquist and Blum, 2007; Blum et al., 2014; Thibodeau and
782 Bergquist, 2017 and references therein).
783 In more detail, deposition of Hg in many terrestrial systems is dominated by
784 gaseous elemental Hg via uptake by vegetation and subsequent litterfall that results in
785 terrestrial biomass and soils acquiring negative MIF and MDF. Thus, marine sediments
786 close to continents and dominated by terrestrial input often reflect this source of Hg. In
787 contrast, marine sediments farther from land that are dominated by atmospheric depositon
788 of HgII species have positive MIF and less negative MDF. Our results for MIF and MDF
789 outside of the ETE are consistent with varying mixtures of Hg sourced from the atmosphere
790 (positive MIF, less negative MDF) and Hg sourced from terrestrial runoff (negative MIF,
791 more negative MDF). The Hg MIF signatures are also consistent with the expectation for
792 the depositional environment of each section — with slightly positive MIF at the deeper
793 (Levanto) section, likely more influenced by atmospherically derived Hg, and more
794 negative MIF at the shallower sections (St. Audrie's Bay, New York Canyon), more
795 influenced by terrestrial sources (Figs. 3–4 and 6). The St. Audrie's Bay section, which is
796 shallow enough to have been exposed subaerially during the ETE, shows the most negative
797 MIF of any section studied here. In summary, when Hg/TOC ratios are relatively low

798 (typically before and after the ETE), each section bears a MIF composition consistent with
799 its major source of Hg input, with near-shore sections displaying terrestrial negative MIF
800 (which may also be related to fires and biomass burning as suggested by Grasby et al.,
801 2019; e.g., at St. Audrie's Bay) and more offshore sections having positive MIF values
802 reflected of atmospheric deposition of HgII species (positive MIF for offshore sections;
803 e.g., Levanto) (Figs 2 and 8).

804 In contrast, when Hg/TOC is elevated during ETE Hg/TOC anomalies, MIF values
805 approach zero, consistent with Hg input from unaltered volcanic sources (Thibodeau and
806 Bergquist, 2017). Importantly, the absence or decrease in the extent of MIF coincides with
807 the intervals of elevated Hg/TOC in each section. When the elevated Hg/TOC periods
808 cease, the two shallower sections also see a return to odd MIF values, although with
809 different timings. At St. Audrie's Bay, the Hg/TOC peak ends relatively abruptly, and
810 negative MIF returns in the first sample measured from the Hettangian. At New York
811 Canyon, there is a somewhat more gradual return to background Hg/TOC extending into
812 the earliest Hettangian, and the absence of MIF follows suit. The Levanto record is
813 different, and exhibits elevated and noisey Hg/TOC persisting throughout the Hettangian
814 and positive MIF does not reoccur after the ETE (discussed in more detail below).
815 Altogether, the disappearance of MIF is remarkably consistent across the three different
816 sections, suggesting that absence or decrease of MIF may be a general feature of TJB Hg
817 anomalies. This observation lends support to a global magmatic source for the Hg
818 anomalies at this time (consistent with the conclusions of Thibodeau et al., 2017).

819 Like the MIF signal, the Hg isotope MDF compositions largely reflect the
820 depositional setting of each section. We observe negative MDF in all sections (Figs 3–4

and 6), but this signature is less pronounced at Levanto, which likely had less relative terrestrial influence relative to St. Audrie's Bay and New York Canyon given its deeper depositional setting and positive MIF values prior to the ETE. Closer proximity to the continents results in more continental influence and more influence from biomass and soil, resulting in more negative MDF compositions. At New York Canyon, there is a general trend towards more negative δ^{202}Hg values coincident with upward shallowing through the section. The increasingly negative δ^{202}Hg values may reflect an increase in the relative amount of continentally derived material versus atmospheric deposition. Unlike the MIF signal, we do not see systematic shifts in δ^{202}Hg values associated with the Hg/TOC anomalies in any of the three sections studied here; this is not surprising given volcanic Hg also has negative MDF that overlaps with terrestrial Hg and atmospheric HgII.

6.2 Comparison to Hg isotope records from other mass extinction and LIP intervals

Mercury isotope records are also available from other sedimentary sections deposited during LIP activity (summarized in Fig. 8). Across these studies, as in the case of the ETE, MIF signatures broadly reflect the depositional setting (e.g., as in Fig. 2). However, the end–Triassic is distinct in that MIF is negligible or shifts towards zero during the Hg/TOC anomaly, at least for the localities studied thus far, while similar systematic shifts are not seen during other time periods. For example, there are several records of Hg isotopes for the end–Permian mass extinction, with several deep-water sections (Buchanan Lake, Sverdrup Basin, Canada; Daxiakou, Shangsi, Gujo-Hachiman) showing positive MIF, and a platform carbonate section (Meishan, China) exhibiting negative MIF, particularly during and after the increase in Hg/TOC (Grasby et al., 2017; Shen et al.,

844 2019b; Wang et al., 2018). However, changes in the MIF signature during the end–Permian
845 Hg/TOC anomaly are inconsistent. At Gujo-Hachiman, MIF decreases much as it does in
846 the end–Triassic sections, but there is little change in MIF of the other end–Permian
847 sections (Buchanan Lake, Xiakou) and a shift from positive to negative MIF is observed at
848 Meishan.

849 The limited Hg isotope data from other time intervals also present a mixed picture.
850 During the Toarcian Ocean Anoxic Event, data from a near-shore section suggest a shift
851 from slightly positive (0.06‰ to 0.07‰) to negative MIF (less than –0.10‰) during the
852 Hg anomaly and carbon isotope excursion (Them et al., 2019). At the Ordovician–Silurian
853 boundary, no significant change in the MIF signal was found during two apparent Hg/TOC
854 anomalies in deep water (Gong et al., 2017) or from S-rich shale sections (Shen et al.,
855 2019a) in China (however, the potential of LIP emplacement at this interval is regarded as
856 circumstantial by some studies; e.g., Shen et al. 2019). Across the Cretaceous–Paleogene
857 transition, the MIF signature during Hg excursions range widely (Sial et al., 2016). In some
858 cases, the lack of consistent isotopic signatures associated with Hg/TOC anomalies might
859 indicate a non-volcanic origin of the anomaly. In other cases, such as during the end–
860 Permian, volcanically derived Hg may have been subject to environmental transformation
861 after its release, imparting characteristic MIF depending on depositional setting (as
862 suggested by Thibodeau and Bergquist, 2017). At the end–Triassic, the rapid volcanic
863 release may have overloaded any MIF-inducing environmental processes prior to
864 deposition. If this interpretation is correct, the new data presented here show that this
865 overloading generated negligible MIF signature in sections across a wide range of

866 depositional settings at the end–Triassic. Determining whether this feature is observed in
867 all end–Triassic localities will require additional analyses.

868 The apparent contrast between the end–Triassic and end–Permian suggests that Hg
869 isotopes may not provide a "smoking gun" to distinguish whether apparent anomalies are
870 associated with LIP-derived Hg (Bergquist, 2017). Yet the differences in Hg behavior
871 between time intervals may also hold general clues about the fate of volatiles released by
872 different LIPs — an important question with implications for the environmental effects and
873 ultimately for the causes of mass extinction. Why the fate of volcanically released Hg might
874 have differed during the end–Permian versus the end–Triassic remains to be understood
875 but raises intriguing questions. For example, was the difference because of more rapid
876 volatile release during CAMP? Or did the Siberian trap emplacement release Hg from coal
877 beds and organic-rich sediments with MIF during the end–Permian? To date, the number
878 of studies reporting Hg isotope data from sedimentary rock records lags far behind those
879 presenting Hg contents and Hg/TOC ratios. Though Hg isotopes are much more
880 challenging to measure, they may offer unique insights that are simply missing from
881 concentration data alone. The consistency of the MIF patterns observed in this study at the
882 end–Triassic suggests that a concerted effort to add isotopic information may be important
883 to realizing the full scope of the Hg proxy.

884

885 **6.3 Elevated volcanogenic Hg persists after CAMP magmatism in some Triassic-**
886 **Jurassic sections**

887 The apparent ubiquity of elevated Hg/TOC during the ETE (Fig. 9; Percival et al.,
888 2017) suggests that elevated Hg may be a global signal during this interval of time,

889 presumably relating to CAMP volatile emissions. However, when viewing the Hg and
890 Hg/TOC 'anomalies' section by section, a number of complexities become apparent. The
891 Levanto section, which has a high-resolution chronology from ash bed U–Pb ages, seemed
892 a promising opportunity for testing the correspondence between CAMP timing (as
893 constrained by the U–Pb age dates) and increases in Hg and Hg/TOC contents. However,
894 Hg contents do not align with CAMP U–Pb ages in this section; instead elevated Hg begins
895 ca. 150 kyrs (ca. 201.5 Ma) after the oldest dated CAMP basalts (Fig. 10; 201.63 ± 0.029
896 Ma; Davies et al., 2017). Meanwhile, the youngest U–Pb dated CAMP basalts are 201.1 ±
897 0.071 Ma, but at the Levanto section elevated Hg persists until the top of the section at ca.
898 200.1 Ma. Similar elevated Hg/TOC also persists into the Early Jurassic in the Lombardy
899 sections (Fig. 9). These mismatches in timing between the Hg signal and CAMP activity
900 are a clear indication that increases in Hg contents and Hg/TOC are imperfect proxies for
901 magmatism in the sedimentary record, especially when looking to this proxy for temporal
902 correlation.

903 The effect of intrusive vs. extrusive magmatism on Hg release (e.g., Percival et al.
904 2017) does not on its own explain the timing discrepancy in the onset of the Hg anomaly
905 from Levanto. The earliest dated phases of CAMP activity were intrusive (Davies et al.,
906 2017), possibly releasing less Hg than expected from extrusive volcanism. However, only
907 the first dated CAMP basalt is intrusive (red CAMP age in Fig. 10), and several ages for
908 CAMP extrusives also pre-date the increase in Hg/TOC seen at Levanto (Fig. 10), requiring
909 another explanation for the mismatch in timing at the onset of the Hg anomaly in this
910 section.

The long persistence of the anomaly at Levanto is also unexpected. Prolonged supply of CAMP-related Hg, e.g., from the continents, could be one explanation. However, if Levanto were receiving Hg from terrestrial runoff, or from atmospheric deposition, we would expect to see a characteristic Hg isotope signal; instead, MIF remains near zero throughout the higher and noiser high Hg/TOC interval. Another explanation would be that CAMP activity lasted longer than suggested by currently available U/Pb dates; however, similar non-MIF, high Hg/TOC samples do not persist into the Hettangian at the St. Audrie's Bay or New York Canyon sections, so it seems unlikely that the long-lasting signal at Levanto simply reflects more CAMP-derived atmospheric Hg deposition extending into the Hettangian.

A more plausible explanation for the extended period of high Hg/TOC at Levanto and the Lombardy basin is that depositional and/or diagenetic processes in the local environments controlled Hg and TOC concentrations. These processes may also explain the delayed onset of the Hg anomaly at Levanto. In the section that follows, we consider these effects more deeply.

6.4 Depositional and diagenetic controls on Hg contents and Hg/TOC ratios in sedimentary rocks

Recent studies have recognized and investigated the importance of the Hg host phase when applying Hg contents and Hg/TOC ratios as a proxy for LIP magmatism (Shen et al., 2019a, b, 2020; Keller et al., 2020; Kovács et al. 2020), as well as the role of weathering in altering depositional Hg contents (Charbonnier et al., 2020). We removed surficial, altered material from our samples and did not observe the kind of systematic

effects anticipated from weathering (Charbonnier et al., 2020), so we do not see weathering as a likely control on the changes in Hg and Hg/TOC observed through the sections we have studied. However, differences in depositional environment likely played an important role. Since the depositional environment and diagenetic history control the presence of the host phases of Hg, they ultimately control the Hg contents. We can therefore expect that Hg concentrations of most if not all sedimentary sections will be primarily controlled by depositional environment and in turn host phases of Hg, and secondarily controlled by secular changes in the global surficial Hg pool.

6.4.1 Plausible host phases for Hg in relation to depositional environment of each section

Each section in this study exhibits a different depositional environment, and in some cases these changed through time. The depositional and diagenetic histories of each section and subsection impacted the TOC, S, clay, and carbonate contents, and thus ultimately the Hg contents. While we lack detailed characterization of Hg associations in each section, we can make some general observations based on Hg-TOC correlations and independent information about each section, such as presence or absence of sulfide minerals. In the New York Canyon section, the host phase for Hg in the post-extinction interval is likely dominantly TOC (based on their close correlation). At St. Audrie's Bay, Hg in likely hosted by TOC. In the Lombardy basin sections, TOC may be the dominant host, although it seems likely that carbonate dilution plays a larger role in the measured Hg contents than at other sections. The Levanto section Hg contents are negatively correlated with carbonates, suggesting dilution may play a major role in determining the Hg contents in these rocks. The host phase for Hg at the Levanto section may be clays, as TOC appears

to play a minor role (based on the low correlations) and there is no evidence abundant S (based on the absence of sulfide phases in thin sections).

6.4.2 Possible paleo-environmental controls on depositional effects

Depth and proximity to continental sources may influence Hg contents in the sedimentary record (e.g., Them et al., 2019; see their fig. 6). The rapid changes in depositional environment seen at shallow sections mean environmental parameters that can affect both Hg and TOC, as well with other rock materials including carbonate, may affect Hg concentrations and Hg/TOC ratios. We illustrate these changes in Fig. 11 and briefly discuss some below, in terms of their potential influence on the ETE Hg records studied here.

Carbonate deposition and diagenesis may have important effects on geochemical proxies, especially in carbonate-rich rocks (typical of many marine sediments), (e.g., Arvidson and Morse, 2014). Dilution occurs whereby increased carbonate content leads to lower TOC and Hg contents. Mercury contents can be calculated on a carbonate-free-basis to correct for dilution (see Fig S4–6), but this correction does not remove the high Hg and Hg/TOC in the Hettangian at Levanto and Lombardy. Another important process in carbonate rich rocks is the migration of carbonate during early diagenesis, possibly leaving organic C and associated Hg behind. In the Hettangian and ETE portions of the Levanto section, Hg is enriched in samples from thin beds with lower carbonate content and depleted in carbonate-rich beds (Fig. SI 5), and carbonate and Hg contents are negatively correlated (Fig. 7h). These patterns could be due to migration of carbonate and/or dilution, but on its own, the bed-to-bed alternating enrichment and depletion does not explain the overall relatively elevated Hg/TOC throughout this interval at Levanto.We note that at any

979 rate these aren't particularly elevated contents (e.g., see fig. 11 from Charbonnier et al.,
980 2020).

981 Processes controlling organic C preservation are also expected to influence
982 Hg/TOC ratios. Organic C in marine sediments is subject to degradation that greatly
983 depends on water depth, local productivity, oxygen exposure time at the sediment water
984 interface, and sedimentary reworking (see also Charbonnier et al., 2020). Changes in depth
985 at St. Audrie's Bay may have contributed to the very low TOC (and potentially high
986 Hg/TOC) during the ETE at this section. Although there is no evidence for similar changes
987 in depth at Levanto that would have led to preferential TOC loss and the observed Hg/TOC
988 enrichment in the Hettangian, it is difficult to rule out all possible changes that could have
989 affected organic C preservation (e.g., Charbonnier et al., 2020).

990 Widespread anoxia and/or euxinia associated with the Triassic–Jurassic boundary
991 (Schootbrugge et al. 2008; Jost et al., 2017), like many other extinction events, may have
992 favored the deposition of sulfides and associated Hg enrichment (e.g., Bower et al., 2008;
993 Han et al., 2014; He et al., 2020). Large sedimentary pyrites are found in the Hettangian at
994 St. Audrie's Bay (Hesselbo et al., 2004; Wignall, 2001). Such an increase in anoxia would
995 likely affect sedimentary S deposition, and therefore may have also affected sedimentary
996 Hg deposition.

997 *6.4.3 Interpretation of Hg/TOC ratios from low-TOC samples*

998 The complexity of host phases and depositional effects on Hg content is magnified
999 when interpreting Hg/TOC ratios in samples with particularly low TOC contents. While
1000 previous studies have regarded high Hg/TOC ratios in samples with TOC <0.2 wt.% as
1001 artifacts (see Section 2.1) or difficult to interpret, we instead suggest that they reflect an

1002 additional, and important, layer of complexity arising from the processes that sequester Hg
1003 and its associated elements in sediments. High Hg/TOC ratios associated with low
1004 TOC content are not artifacts per se, in that they do represent Hg enrichment relative to
1005 TOC. However, at low TOC values, small changes in TOC can lead to large changes in
1006 Hg/TOC despite little change in Hg contetns. The more relevant question is whether these
1007 represent the enrichment of Hg in association with TOC, or the increasing importance of
1008 Hg hosted in other phases — emphasizing the need to better understand Hg distribution in
1009 sedimentary rocks, especially in those with low TOC content (see also Shen et al., 2020).
1010 Recent studies have greatly expanded our understanding of the role of S sequestration in
1011 Hg 'anomalies' (Shen et al., 2019a; Shen et al., 2020), and demonstrated that sediments
1012 deposited in highly-reducing, highly sulfidic environments sequester Hg to an extent that
1013 obscures any global Hg signal (Shen et al., 2019a). Similar micro-scale study of carbonate-
1014 rich, sulfide-poor lithologies such as those from Levanto and the Lombardy Basin could
1015 help illuminate the controls on Hg distribution in these low TOC rocks.

1016 *6.4.4 Summary of depositional effects*

1017 Mercury records in marine sedimentary rocks across the ETE, and at other
1018 extinction events, are likely affected by a combination of all the processes discussed above.
1019 Ocean anoxia and euxinia (from CO_2-induced global warming and increased nutrient
1020 runoff), increased Hg, and increased S are all possible direct and indirect consequences of
1021 CAMP, and elevated Hg and Hg/TOC may be affected by a combination of these effects.
1022 Further, changes in the carbonate system (e.g., Greene et al., 2012), global redox (e.g.,
1023 Schootbrugge et al., 2013; Kasprak et al., 2015; Jost et al., 2017) or changes in delivery of
1024 clay (e.g., from increased weathering) are all downstream consequences of LIP magmatism

1025 that also could have impacted Hg delivery and/or preservation. Thus we expect a general
1026 connection between LIP activity and Hg, as observed consistently in our ETE sections, but
1027 the causes of that enrichment, and the timing of Hg anomalies, may be complex. Notably,
1028 the persistent Hg enrichment in the Hettangian that we see at both Levanto and Lombardy
1029 seems difficult to explain by one depositional effect alone, since the elevated Hg/TOC
1030 ratios are observed in carbonate-rich, low-TOC samples in Lombardy but the carbonate-
1031 poor, higher TOC samples from the Hettangian at Levanto.

1032 Better understanding of depositional effects, and distinguishing between them, may
1033 provide a more robust foundation for using Hg contents as a proxy for magmatism. What
1034 is clear is that the relatively poor correspondence between CAMP dates and the timing of
1035 the Hg/TOC anomaly at Levanto casts doubt the use of Hg contents from a single site to
1036 fingerprint the timing of discrete pulses of magmatism directly (cf. Percival et al., 2017),
1037 at least in the absence of independent constraints on sedimentary reworking of Hg.

1038

1039 **6.5 Next steps**

1040 Our examination of Hg in different depositional environments across the Triassic–
1041 Jurassic boundary corroborates other recent studies noting the complexity in depositional
1042 and diagenetic controls on Hg concentrations and Hg/TOC ratios in sedimentary rocks
1043 (Faggetter et al., 2019; Percival et al., 2018; Shen et al., 2019a,b, 2020; Them et al., 2019;
1044 Charbonnier et al., 2020). At the same time, our results show that, despite the complexity,
1045 there may be a reliable signal of CAMP magmatism recorded by the combination of
1046 Hg/TOC and Hg isotopes across a range of depositional environments at the end–Triassic.
1047 When considered together, Hg isotopes and contents may provide valuable information

about LIP magmatism in sedimentary sections, but the numerous processes influencing Hg contents and Hg/TOC ratios suggest caution is warranted when applying these measurements alone, especially when using single-site records and when seeking to identify detailed timing.

Future studies of the Hg proxy in deep time should aim to investigate where in the rock Hg is found, specifically what minerals host Hg and what other elements it is associated with in each sample (e.g., organic C versus S; Shen et al., 2020). As suggested by Grasby et al. (2019), total S measurements may help elucidate the role of S sequestration in the Hg anomalies. Similarly, carefully relating Hg contents and Hg/TOC ratios to other geochemical records (e.g., of local anoxia), as well as investigating sequence stratigraphic changes within a record, provide opportunities for better informing interpretation of apparent Hg anomalies. Further understanding may come from exploring more Hg records when LIP magmatism is not expected. Finally, more connection to research on Hg in modern marine sediments could help to elucidate how Hg is delivered to and preserved in sedimentary environments.

7. CONCLUSIONS

We studied five sections spanning the Triassic–Jurassic boundary, and in the four sections with measurable Hg (excluding the carbonate platform of Mt. Sparagio (Sicily) which had Hg below the detection limit), Hg/TOC increases in association with the ETE and CAMP emplacement. At New York Canyon and St. Audrie's Bay, peaks in Hg/TOC are well defined and correspond well with the timing of the end–Triassic extinction as inferred from stratigraphic relationships and organic C isotopes. In contrast, at the Levanto

and Lombardy sections, Hg/TOC remains elevated for much longer, well into the Hettangian. The well-constrained absolute chronology from Levanto shows that the long-lasting elevated Hg/TOC persists well after the youngest U–Pb date of CAMP activity. These results suggest abundant caution is needed when inferring the timing of mass volcanism from Hg anomalies in sedimentary rocks, particularly from a single stratigraphic section, and in the example studied here, even with the benefit of multiple sections.

Mercury isotope signatures across the studied sections are consistent with the expected signatures based on each site's depositional environment. Shallow, nearshore sites have negative δ^{202}Hg and Δ^{199}Hg values, and the New York Canyon data are consistent with existing interpretations of shallowing upwards at this locality. In the deeper basinal setting of Levanto, slightly positive MIF are indicative of an atmospheric and marine-influenced Hg source, but δ^{202}Hg values suggest some continental influence on MDF signatures. At each site, MIF is near or approaches zero during the ETE and CAMP magmatism, supporting the idea that a large source of volcanic Hg may have overwhelmed the surficial Hg cycle at the time, leading to a notable reduction in the Hg MIF signature recorded in sedimentary rocks. Differences between Hg isotope behavior during this time interval versus the end-Permian raise the intriguing possibility of whether Hg isotopes offer clues about volatile recycling associated with massive volcanism in the geologic past. Overall, our work suggests that, despite the complex processes that are increasingly recognized as influencing sedimentary Hg records, the Hg proxy can still be informative — but that it can be most reliably applied by studying sections that span diverse depositional environments and by including measurements of Hg isotope ratios as well as concentrations.

Acknowledgements

This project was funded by the National Science Foundation Earth-Life Transitions program (NSF award 1338329) and Canadian programs NSERC-Discovery, RGPIN355617-552-2008; CIFAR-ESEP). Manuel Rigo was supported by the grants PRIN 2017W2MARE. Laura Zimmerman was supported by the Canadian NSERC USRA program. Sarah E. Greene was supported by NERC Independent Research Fellowship NE/L011050/1 while working on this manuscript. We thank Renée Z. Wang for help sampling the New York Canyon upper samples. Melissa Zepeda and Reyna Ibarra, two high school students from the University of Southern California Young Researcher's Program, are thanked for their efforts related to this work. Joyce Ann Yager acknowledges funding from the Elizabeth and Jerol Sonosky Fellowship at USC. We gratefully acknowledge the editorial handling and comments from Shane Schoepfer and Thomas Algeo as well as the helpful comments from Jun Shen and those from an anonymous reviewer that helped us produce a more incisive and clear manuscript; the comments from two anonymous reviewers on an earlier version of the manuscript also aided in producing a more succinct manuscript.

FIGURE CAPTIONS

Fig. 1. [A] [A] Late Triassic paleogeography with paleogeographic locations of studied sections, adapted from Kuroda et al. (2010). 1: St. Audrie's Bay, UK; 2: New York Canyon, Nevada; 3: Lombardy Basin, Italy; 4: Mt. Sparagio, Sicily, Italy; 5: Levanto, Peru. [B] Relative depositional settings of study sites and expected Hg, TOC, and Hg isotope data at

each site based on relative depth and energy of environment. This is a simplified representation of how Hg enters the marine record, with particular attention to Hg isotopes and relative contributions based on proximity to the continent and depth, and these sites were thousands of kms apart during actual deposition. Based on Thibodeau and Bergquist (2016) and references therein.

Figure 2. Carbon isotope correlation of sections studied here. Mt. Sparagio data and stratigraphic column is from Todaro et al. (2018); Lombardy basin data is from Zaffani et al. (2018), Bachan et al. (2012), and this study; St. Audrie's Bay data is from this study and stratigraphic column is from Hesselbo et al. (2004); New York Canyon data is from Thibodeau et al. (2017) and this study; Levanto data is from Yager et al. (2017). Note that this correlation forms the basis for Fig. 9. Gray shape denotes the initial negative isotope excursion. Triassic–Jurassic boundary is placed at the first occurrence of *P. spelae* for the Levanto and New York Canyon sections and is based on Todaro et al. (2018), Zaffani et al. (2018), and Hesselbo et al. (2004) for the Mt. Sparagio, Lombardy basin, and St. Audrie's bay sections, respectively.

Figure 3. Stratigraphic column from New York Canyon, Nevada (Corsetti et al. 2015) with δ^{13}Corg, Hg, TOC, Hg/TOC, δ^{202}Hg (MDF), and Δ^{199}Hg (MIF, vertical gray bar denotes no MIF) from this study and Thibodeau et al. (2016). Horizontal gray bar denotes ETE. Colored bar on Hg/TOC plot adapted from fig. 12 of Charbonnier et al. (2020), and provides relative guide for Hg/TOC anomalies.

Figure 4. Stratigraphic column from St. Audrie's Bay, UK (Hesselbo et al. 2004) with δ^{13}Corg, Hg, TOC, Hg/TOC, δ^{202}Hg (MDF), and Δ^{199}Hg (MIF, vertical gray bar denotes no MIF) from this study. Horizontal gray bar denotes ETE. "Will" refers to Williton member; "Lils." Refers to Lilstock Fm. Horizontal gray bar denotes ETE. Mercury data from Percival et al. (2017) and Hg/TOC data (calculated from Hesselbo et al., 2002 and Percival et al., 2017) are also shown. Note that TOC data was measured using different methods. The discrepancies between both sections in TOC measurements, particularly in the Lilstock formation, result in a large discrepancy between Hg/TOC measurements. These may be due to TOC methodologies, heterogeneity in the section from bed to bed, or both. Colored bar in Hg/TOC plot as in Fig. 3.

Figure 5. Composite stratigraphic heights from Italian sections (for lithologic logs for individual sections, see SI Fig. 2). Formation name and section name are displayed, with δ^{13}Corg, Hg, TOC and Hg/TOC. Zu = Calcari di Zu Formation; M = Malanotte Formation; Moltrasio = Calcare di Moltrasio Fm; stratigraphic logs are based on Galli et al. (2007), Jadoul et al. (2012), Zaffani et al. (2018), and this study. Horizontal gray bar denotes ETE. Colored bar in Hg/TOC plot as in Fig. 3.

Fig. 6. Stratigraphic column from Levanto, Peru (Yager et al., 2017) with δ^{13}Corg, Hg, TOC, CC, Hg/TOC, δ^{202}Hg (MDF), and Δ^{199}Hg (MIF; vertical gray bar denotes no MIF) from this study. Horizontal gray bar denotes ETE. Colored bar in Hg/TOC plot as in Fig. 3.

Fig. 7. Hg/TOC data and Hg isotope data (MIF) plotted with stratigraphy for St. Audrie's Bay, Levanto, and New York Canyon related based on organic C isotope correlation; horizontal gray bars indicate ETE. Stratigraphic column for New York Canyon is from Thibodeau et al. (2016); stratigraphic column from St. Audrie's Bay is from Hesselbo et al. (2004); stratigraphic column from Levanto is from Yager et al. (2017). Data from the lower portion of the New York Canyon section is from Thibodeau et al. (2016).

Fig. 8. Summary of Hg isotope data in this and previous studies.

Fig. 9. Hg and Hg/TOC from this study with summary of anoxia/euxinia proxies. Gray bar denotes ETE based on the initial carbon isotope excursion in Fig. 2. Black boxes denote possible euxinia at those sections, which do not align with high Hg/TOC or Hg or at a single point in time. Mt. Sparagio is from $\delta^{34}S_{cas}$ data from He et al. (2020); Lombardy basin data is from $\delta^{238}U$ from Jost et al. (2017); St. Audrie's Bay data is from pyrite framboids reported in Hesselbo et al. (2004); New York Canyon data is from Larina et al. (unpublished data); Levanto data is from Yager et al. (unpublished data).

Fig. 10. Levanto section Hg/TOC data (this study) plotted using the age model from Yager et al. (2017) and displayed with CAMP U–Pb age dates from Davies et al. (2017). High Hg/TOC was expected to overlap with CAMP U–Pb ages, but elevated Hg persists for much longer and does not begin coincident with the earliest known CAMP ages.

1185 **Fig. 11.** Schematic displaying example ways LIP magmatism may impact the Hg cycle
1186 with respect to measured Hg contents and Hg/TOC.
1187

REFERENCES

Antonelli, M., Franciosi, R., Pezzi, G., Querci, A., Ronco, G.P., Vezzani, F., 1988. Paleogeographic Evolution and structural setting of the northern side of the Sicily Channel. Mem. della Soc. Geol. Ital. 41, 141–157.

Arvidson, R.S., Morse, J.W. 2014.

Bachan, A., Van De Schootbrugge, B., Fiebig, J., McRoberts, C.A., Ciarapica, G., Payne, J.L., 2012. Carbon cycle dynamics following the end-Triassic mass extinction: Constraints from paired δ^{13}C<inf>carb</inf> and δ^{13}C<inf>org</inf> records. Geochemistry, Geophys. Geosystems. https://doi.org/10.1029/2012GC004150

Barattolo, F., Romano, R., 2005. Shallow carbonate platform bioevents during the Upper Triassic-Lower Jurassic: An evolutive interpretation. Boll. della Soc. Geol. Ital. 124, 123–142.

Bartolini, A., Guex, J., Spangenberg, J.E., Schoene, B., Taylor, D.G., Schaltegger, U., Atudorei, V., 2012. Disentangling the Hettangian carbon isotope record: Implications for the aftermath of the end-Triassic mass extinction. Geochemistry, Geophys. Geosystems 13, Q01007. https://doi.org/10.1029/2011GC003807

Berner, R.A., Beerling, D.J., 2007. Volcanic degassing necessary to produce a CaCO3 undersaturated ocean at the Triassic-Jurassic boundary. Paleogeogr. Paleoclimatol. Palaeoecol. 244 (1-4), 368-373.

Bergquist, B.A., Blum, J.D., 2007. Mass-dependent and -independent fractionation of Hg isotopes by photoreduction in aquatic systems. Science (80-.). 318, 417–420. https://doi.org/10.1126/science.1148050

Bergquist, B.A., 2017. Mercury, volcanism, and mass extinctions. Proc. Natl. Acad. Sci. U. S. A. 114 (33) 8675-8677.

Bersezio, R., Jadoul, F., Chinaglia, N., 1997. Geological map of the Norian-Jurassic succession of the Southern Alps North of Bergamo. An explanatory note. Boll. Soc. Geol. It. 116, 363–378.

Blackburn, T. J. et al. Zircon U-Pb geochronology links the end-Triassic extinction with the Central Atlantic magmatic province. Science 340, 941–945 (2013).

Blum, J.D., and Bergquist, B.A., 2007, Reporting the variations in the natural isotopic composition of mercury, Anal Bioanal Chem, v. 388, p. 353-359, doi: 10.1007/s00216-007-1236-9.

Blum, J.D., Sherman, L.S., Johnson, M.W., 2014. Mercury Isotopes in Earth and Environmental Sciences. Annu. Rev. Earth Planet. Sci. https://doi.org/10.1146/annurev-earth-050212-124107

Bond, D.P.G., Wignall, P.B., 2014. Large igneous provinces and mass extinctions: An update. Spec. Pap. Geol. Soc. Am. https://doi.org/10.1130/2014.2505(02)

BouDagher-Fadel, M.K., Bosence, D.W.J., 2007. Early Jurassic benthic foraminiferal diversification and biozones in shallow-marine carbonates of western Tethys. Senckenbergiana lethaea 87, 1–39. https://doi.org/10.1007/BF03043906

Bown, P., Morton, N., Lees, J., 2007. Newsletter: International Subcomission on Jurassic Stratigraphy v. 34, p. 1–72.

Bower, J., Savage, K.S., Weinman, B., Barnett, M.O., Hamilton, W.P., Harper, W.F., 2008. Immobilization of mercury by pyrite (FeS2). Environ. Pollut. 156 (2), 504–514.

Cacciatore, M.S., Di Stefano, P., Rettori, R., 2006. Carbonate platform-basin systems in Sicily around the Triassic/Jurassic boundary: new data from the Campofiorito area (Sicani Mountains, western Sicily). Quad. del Mus. Geol. Gemmellaro 9, 41–54.

Charbonnier, G., Adatte, T., Fölmi, K. B., Suan, G., 2020. Effect of intense weathering and postdepositional degredation of organic matter on Hg/TOC proxy in organic-rich sediments and its implications for deep-time investigations. Geochem., Geophys., Geosyst. 21 doi: 10.1029/2019GC008707

Corsetti, F. A., Ritterbush, K. A., Bottjer, D. J., Greene, S. E., Ibarra, Y., Yager, J. A., West, A. J., Berelson, W. M., Rosas, S., Becker, T. W., Levine, N. M., Loyd, S. J., Martindale, R. C., Petryshyn, V. A., Carroll, N. R., Petsios, E., Piazza, O., Pietsch, C., Stellmann, J. L., Thompson, J. R., Washington, K. A., Wilmeth, D. T., 2015, Investigating the Paleoecological Consequences of Supercontinent Breakup: Sponges Clean Up in the Early Jurassic. The Sedimentary Record 13:2.

D'Argenio, B., 1974. Le piattaforme carbonatiche Periadriatiche: una rassegna di problemi nel quadro geodinamico Mesozoico dell'area Mediterranea. Mem. della Soc. Geol. Ital. 13 (Suppl., 1–28.

Davies, J.H.F.L., Marzoli, A., Bertrand, H., Youbi, N., Ernesto, M., Schaltegger, U., 2017. End-Triassic mass extinction started by intrusive CAMP activity. Nat. Commun. https://doi.org/10.1038/ncomms15596

Demers, J.D., Blum, J.D., Zak, D.R., 2013. Mercury isotopes in a forested ecosystem: implications for air-surface exchange dynamics and the global mercury cycle. Glob. Biogeochem. Cycles 27 (1), 222–238.

Di Stefano, P., Favara, R., Luzio, D., Renda, P., Cacciatore, M.S., Calò, M., Napoli, G., Parisi, L., Todaro, S., Zarcone, G., 2015. A regional-scale discontinuity in western Sicily revealed by a multidisciplinary approach: A new piece for understanding the geodynamic puzzle of the southern Mediterranean. Tectonics. https://doi.org/10.1002/2014TC003759

Douglas, T.A., Sturm, M., Simpson, W.R., Blum, J.D., Alvarez-Aviles, L., Keeler, G.J., Perovich, D.K., Biswas, A., Johnson, K., 2008. Influence of snow and ice crystal formation and accumulation on mercury deposition to the arctic. Environ. Sci. Technol. https://doi.org/10.1021/es070502d

Elderfield, H., 2002. Foraminiferal Mg/Ca Paleothermometry: Expected Advances and Unexpected Consequences. Geochim. Cosmochim. Acta 66 Supplem, 213.

Faggetter, L.E., Wignall, P.B., Pruss, S.B., Jones, D.S., Grasby, S., Widdowson, M., Newton, R.J., 2019. Mercury chemostratigraphy across the Cambrian Series 2 – Series 3 boundary: evidence for increased volcanic activity coincident with extinction? Chem. Geol. https://doi.org/10.1016/j.chemgeo.2019.02.006

Fitzgerald et al 2014 (treatise)

Foster G.L., Hull, P., Lunt, D.J., Zachos, J.C. 2018 Placing our current 'hyperthermal' in the context of rapid climate change in our geological past. *Phil. Trans. R. Soc. A* **376**: 20170086. http://dx.doi.org/10.1098/rsta.2017.0086

Fox, C. P., Cui, X., Whiteside, J. H., Olsen, P.E., Summons, R.E., Grice, K. 2020. Molecular and isotopic evidence reveals end-Triassic carbon isotope excursion is not from massive exogenous light carbon. Prococeedings of the National Academey of Sciences. /doi/10.1073/pnas.1917661117

1279 Galli, M.T., Jadoul, F., Bernasconi, S.M., Weissert, H., 2005. Anomalies in global carbon
1280 cycling and extinction at the Triassic/Jurassic boundary: evidence from a marine C-
1281 isotope record. Palaeogeogr. Palaeoclimatol. Palaeoecol. 216, 203–214.
1282 Galli, M.T., Jadoul, F., Bernasconi, S.M., Cirilli, S., Weissert, H., 2007. Stratigraphy and
1283 palaeoenvironmental analysis of the Triassic-Jurassic transition in the western
1284 Southern Alps (Northern Italy). Palaeogeogr. Palaeoclimatol. Palaeoecol.
1285 https://doi.org/10.1016/j.palaeo.2006.06.023
1286 Galy, V., Bouchez, J., France-Lanord, C., 2007. Determination of total organic carbon
1287 content and δ13C in carbonate-rich detrital sediments. Geostand. Geoanalytical Res.
1288 https://doi.org/10.1111/j.1751-908X.2007.00864.x
1289 Galy, V., Beyssac, O., France-Lanord, C., Eglinton, T. 2008. Recycling of graphite
1290 during Himalayan erosion: A geological stabilization of carbon in the crust. Science
1291 322: 943–945; doi 10.1126/science.1161408.
1292 Gill, G.A., Fitzgerald, W.F., 1988. Vertical mercury distributions in the oceans. Geochim.
1293 Cosmochim. Acta. https://doi.org/10.1016/0016-7037(88)90240-2
1294 Gong, Q., Wang, X., Zhao, L., Grasby, S.E., Chen, Z.Q., Zhang, L., Li, Y., Cao, L., Li,
1295 Z., 2017. Mercury spikes suggest volcanic driver of the Ordovician-Silurian mass
1296 extinction. Sci. Rep. https://doi.org/10.1038/s41598-017-05524-5
1297 Grasby, S.E., Beauchamp, B., Bond, D.P.G., Wignall, P.B., Sanei, H., 2016. Mercury
1298 anomalies associated with three extinction events (Capitanian Crisis, Latest Permian
1299 Extinction and the Smithian/Spathian Extinction) in NW Pangea. Geol. Mag.
1300 https://doi.org/10.1017/S0016756815000436
1301 Grasby, S.E., Sanei, H., Beauchamp, B., Chen, Z., 2013. Mercury deposition through the
1302 Permo-Triassic Biotic Crisis. Chem. Geol.
1303 https://doi.org/10.1016/j.chemgeo.2013.05.022
1304 Grasby, S.E., Shen, W., Yin, R., Gleason, J.D., Blum, J.D., Lepak, R.F., Hurley, J.P.,
1305 Beauchamp, B., 2017. Isotopic signatures of mercury contamination in latest
1306 Permian oceans. Geology. https://doi.org/10.1130/G38487.1
1307 Grasby, S.E., Them, T.R., Chen, Z., Yin, R., Ardakani, O.H., 2019. Mercury as a proxy
1308 for volcanic emissions in the geologic record. Earth-Science Rev.
1309 https://doi.org/10.1016/j.earscirev.2019.102880
1310 Greene, S.E., Martindale, R.C., Ritterbush, K.A., Bottjer, D.J., Corsetti, F.A., Berelson,
1311 W.M., 2012. Recognising ocean acidification in deep time: An evaluation of the
1312 evidence for acidification across the Triassic-Jurassic boundary. Earth-Science Rev.
1313 https://doi.org/10.1016/j.earscirev.2012.03.009
1314 Guex, J., Bartolini, A., Atudorei, V., Taylor, D., 2004. High-resolution ammonite and
1315 carbon isotope stratigraphy across the Triassic-Jurassic boundary at New York
1316 Canyon (Nevada). Earth Planet. Sci. Lett. https://doi.org/10.1016/j.epsl.2004.06.006
1317 Guex, J., Schoene, B., Bartolini, A., Spangenberg, J., Schaltegger, U., O'Dogherty, L.,
1318 Taylor, D., Bucher, H., Atudorei, V., 2012. Geochronological constraints on post-
1319 extinction recovery of the ammonoids and carbon cycle perturbations during the
1320 Early Jurassic. Palaeogeogr. Palaeoclimatol. Palaeoecol.
1321 https://doi.org/10.1016/j.palaeo.2012.04.030
1322 Hallam, A., 1995. Oxygen-restricted facies of the basal jurassic of north west europe.
1323 Hist. Biol. https://doi.org/10.1080/10292389509380523
1324 Hallam, A., 1964. Origin of the Limestone-Shale Rhythm in the Blue Lias of England: A

Composite Theory. J. Geol. https://doi.org/10.1086/626974
Hallam, A., 1960. The White Lias of the Devon coast. Proc. Geol. Assoc. https://doi.org/10.1016/S0016-7878(60)80031-4
Han, D.S., Orillano, M., Khodary, A., Duan, Y., Batchelor, B., Abdel-Wahab, A., 2014. Reactive iron sulfide (FeS)-supported ultrafiltration for removal of mercury (Hg(II)) from water. Water Res. 53, 310–321.
He, T., Dal Corso, J., Newton, R.J., Wignall, P.B., Mills, B.J.W., Todaro, S., Di Stefano, P., Turner, E.C., Jamieson, R.A., Randazzo, V., Rigo, M., Jones, R.E., Dunhill, A. 2020. An enormous sulfur isotope excursion indicates marine anoxia during the end-Triassic mass extinction. Sciences advances. Vol. 6, no. 37, DOI: 10.1126/sciadv.abb6704
DOI: 10.1126/sciadv.abb6704
Hesselbo, S.P., Robinson, S.A., Surlyk, F., 2004. Sea-level change and facies development across potential Triassic-Jurassic boundary horizons, SW Britain. J. Geol. Soc. London. https://doi.org/10.1144/0016-764903-033
Hilton, R.G., Galy, A., Hovius, N., Horng, M.-J., Chen, H. 2010. The isotopic composition of particulate organic carbon in mountain rivers of Taiwan. Geochemica et Cosmochimica Acta 74: 3164–3181. doi: 10.1016/j.gca.2010.03.004.
Huerta-Diaz, M.A., Morse, J.W., 1992. Pyritization of trace metals in anoxic marine sediments. Geochim. Cosmochim. Acta. https://doi.org/10.1016/0016-7037(92)90353-K
Ibarra, Y, Corsetti, F.A., Greene, S., and Bottjer, D. (2016) A microbial carbonate response in synchrony with the end-Triassic mass extinction across the SW UK, Scientific Reports (Nature Publishing Group) v. 6, 19808. http://doi.org/10.1038/srep19808.
Jadoul, F., Galli, M.T., Muttoni, G., Rigo, M., Cirilli, S., 2012. The late Norian-Hettangian stratigraphic and paleogeographic evolution of the Bergamasc Alps. GFT - Geol. F. TRIPS 4, 55.
Jost, A. B., A. Bachan, B. van de Schootbrugge, K. V. Lau, K. L. Weaver, K. Maher, and J. L. Payne (2017), Uranium isotope evidence for an expansion of marine anoxia during the end-Triassic extinction, Geochem. Geophys. Geosyst., 18, doi:10.1002/2017GC006941.
Kasprak, A. H., Sepúlveda, J., Price-Waldman, R., Williford, K. H., Schoepfer, S. D., Haggart, J. W., Whiteside, J. H. 2015, *Episodic photic zone euxinia in the northeastern panthalassic ocean during the end-triassic extinction*. Boulder: Geological Society of America, Inc. doi:10.1130/G36371.1
Keller, G., Mateo, P., Monkenbusch, J., Thibault, N., Punekar, J., Spangenberg, J.E., Abramovich, S., Ashckenazi-Polivoda, S., Schoene, B., Eddy, M.P., Samperton, K. M., Khadri, S. F. R., Adatte, T. 2020. Global and Planetary Change. 194: 103312; doi: 10.1016/j.gloplacha.2020.103312
Kiessling, W., Aberhan, M., Brenneis, B., Wagner, P.J., 2007. Extinction trajectories of benthic organisms across the Triassic-Jurassic boundary. Palaeogeogr. Palaeoclimatol. Palaeoecol. https://doi.org/10.1016/j.palaeo.2006.06.029
Knight, K. B. et al. The Central Atlantic Magmatic Province at the Triassic–Jurassic boundary: paleomagnetic and 40Ar/39Ar evidence from Morocco for brief, episodic volcanism. Earth Plant. Sci. Lett. 228, 143–160 (2004).

1371 Kongchum, M., Hudnall, W.H., DeLaune, R.D., 2011, Relationship between sediment
1372 clay minerals and total, v. 46, p. 534-539, doi: 10.1080/10934529.2011.551745.
1373 Kovács, E. B., Ruhl, M., Demény, A., Fórizs, I., Hegyi, I., Horváth-Kostka, Z. R.,
1374 Móricz, F., Vallner, Z., Pálfy, J. 2020. Mercury anomalies and carbon isotope
1375 excursions in the western tethyan Csővár section support the link between CAMP
1376 volcanism and the end-Triassic extinction. Global and Planetary Change. 194;
1377 103291. doi: 10.1016/j.gloplacha.2020.103291.
1378 Kuroda, J., Hori, R. S., Suzuki, K., Grocke, D. R., Ohkouchi, N., 2010. Marine osmium
1379 isotope record across the Triassic-Jurassic boundary from a Pacific pelagic site.
1380 Geology 38, p. 1095-1098, doi: 10.1130/G31223:1.
1381 Larina, L., Bottjer, D. J., Corsetti, F. A., Thibodeau, A. M., Berelson, W. M., West, A. J.,
1382 Yager, J. A. High-resolution record of environmental change in the lead-up to the
1383 end-Triassic mass extinction. *In review*.
1384 Lindberg, S.E., Brooks, S., Lin, C.J., Scott, K.J., Landis, M.S., Stevens, R.K., Goodsite,
1385 M., Richter, A., 2002. Dynamic oxidation of gaseous mercury in the arctic
1386 troposphere at polar sunrise. Environ. Sci. Technol.
1387 https://doi.org/10.1021/es0111941
1388 Lindström, S., van de Schootbrugge, B.,Dybkjaer, K., Pederson, K. G., Fiebig, J.,
1389 Nielsen, L. H., Richoz, S., 2012, No causal link between terrestrial ecosystem
1390 change and methane release during the end-Triassic mass extinction, Geology, v. 40,
1391 no. 6, p. 531-534, doi: 10.1130/G32928.1.
1392 Lindström et al., 2019, Volcanic mercury and mutagenesis in land plants during the end-Triassic
1393 mass extinction, Science Advances, 5:eaaw4018.Lo Cicero, G., 1986. Carbon and
1394 oxygen isotopic composition of Norian sediments. Panormide Carbonate Platform,
1395 Palermo. Rend Soc Geol It 9, 209–218.
1396 Manceau, A., Merkulova, M., Murdzek, M., Batanova, V., Baran, R., Glatzel, P., Saikia,
1397 B.K., Paktunc, D., Lefticariu, L., 2018. Chemical Forms of Mercury in Pyrite:
1398 Implications for Predicting Mercury Releases in Acid Mine Drainage Settings.
1399 Environ. Sci. Technol. https://doi.org/10.1021/acs.est.8b02027
1400 Marzoli, A., Bertrand, H., Knight, K.B., Cirilli, S., Buratti, N., Vérati, C., Nomade, S.,
1401 Renne, P.R., Youbi, N., Martini, R., Allenbach, K., Neuwerth, R., Rapaille, C.,
1402 Zaninetti, L., Bellieni, G., 2004. Synchrony of the Central Atlantic magmatic
1403 province and the Triassic-Jurassic boundary climatic and biotic crisis. Geology.
1404 https://doi.org/10.1130/G20652.1
1405 Marzoli, A., Renne, P.R., Piccirillo, E.M., Ernesto, M., Bellieni, G., De Min, A., 1999.
1406 Extensive 200-million-year-old continental flood basalts of the Central Atlantic
1407 Magmatic Province. Science (80-.). https://doi.org/10.1126/science.284.5414.616
1408 Mayall, M.J., 1981. The Late Triassic Blue Anchor Formation and the initial Rhaetian
1409 marine transgression in south-west Britain. Geol. Mag.
1410 https://doi.org/10.1017/S0016756800032246
1411 Morton, N., Hesselbo, S., Eds., 2008, Newsletter: International Subcommission on
1412 Jurassic Stratigraphy, v. 35, p. 1–76.
1413 Muttoni, G., Kent, D. V., Jadoul, F., Olsen, P.E., Rigo, M., Galli, M.T., Nicora, A., 2010.
1414 Rhaetian magneto-biostratigraphy from the Southern Alps (Italy): Constraints on
1415 Triassic chronology. Palaeogeogr. Palaeoclimatol. Palaeoecol.
1416 https://doi.org/10.1016/j.palaeo.2009.10.014
1417 Patacca, E., Scandone, P., Giunta, G., Liguori, V., 1979. Mesozoic paleo-tectonic

evolution of the Ragusa zone (southeastern Sicily). Geol. Rom 18, 331–369.
Percival, L.M.E., Jenkyns, H.C., Mather, T.A., Dickson, A.J., Batenburg, S.J., Ruhl, M., Hesselbo, S.P., Barclay, R., Jarvis, I., Robinson, S.A., Woelders, L., 2018. Does large igneous province volcanism always perturb the mercury cycle? Comparing the records of Oceanic Anoxic Event 2 and the end-cretaceous to other Mesozoic events. Am. J. Sci. https://doi.org/10.2475/08.2018.01
Percival, L.M.E., Ruhl, M., Hesselbo, S.P., Jenkyns, H.C., Mather, T.A., Whiteside, J.H., 2017. Mercury evidence for pulsed volcanism during the end-Triassic mass extinction. Proc. Natl. Acad. Sci. U. S. A. https://doi.org/10.1073/pnas.1705378114
Percival, L.M.E., Witt, M.L.I., Mather, T.A., Hermoso, M., Jenkyns, H.C., Hesselbo, S.P., Al-Suwaidi, A.H., Storm, M.S., Xu, W., Ruhl, M., 2015. Globally enhanced mercury deposition during the end-Pliensbachian extinction and Toarcian OAE: A link to the Karoo-Ferrar Large Igneous Province. Earth Planet. Sci. Lett. https://doi.org/10.1016/j.epsl.2015.06.064
Pyle, D.M., Mather, T.A., 2003. The importance of volcanic emissions for the global atmospheric mercury cycle. Atmos. Environ. https://doi.org/10.1016/j.atmosenv.2003.07.011
Richardson, L., 1911. The rhætic and contiguous deposits of west, mid, & part of East Somerset. Q. J. Geol. Soc. London. https://doi.org/10.1144/GSL.JGS.1911.067.01-04.03
Richardson, L., 1906. On the Rhætic and contiguous deposits of Devon and Dorset. Proc. Geol. Assoc. https://doi.org/10.1016/S0016-7878(06)80067-2
Richardson, L., 1905. The Rhætic and contiguous deposits of Glamorganshire. Q. J. Geol. Soc. London. https://doi.org/10.1144/GSL.JGS.1905.061.01-04.20
Ritterbush, K.A., Bottjer, D.J., Corsetti, F.A., Rosas, S., 2014. NEW EVIDENCE ON THE ROLE OF SILICEOUS SPONGES IN ECOLOGY AND SEDIMENTARY FACIES DEVELOPMENT IN EASTERN PANTHALASSA FOLLOWING THE TRIASSIC-JURASSIC MASS EXTINCTION. Palaios. https://doi.org/10.2110/palo.2013.121
Ruhl, M., Kürschner, W.M., Krystyn, L., 2009. Triassic-Jurassic organic carbon isotope stratigraphy of key sections in the western Tethys realm (Austria). Earth Planet. Sci. Lett. https://doi.org/10.1016/j.epsl.2009.02.020
Ruhl, M., Hesselbo, S. P., Al-Suwaidi, A., Jenkyns, H. C., Damborenea, S. E., Manceñido, M. O., Storm, M., Mather, T. A., Riccardi, A. C. 2020. On the onset of Central Atlantic magmatic province (CAMP) volcanism and environmental and carbon-cycle change at the Triassic–Jurassic transition (Neuquén Basin, Argentina). Earth-Science Reviews 208: 103229. doi: 10.1016/j.earscirev.2020.103229.
Sanei, H., Grasby, S.E., Beauchamp, B., 2012. Latest permian mercury anomalies. Geology. https://doi.org/10.1130/G32596.1
Scaife, J.D., Ruhl, M., Dickson, A.J., Mather, T.A., Jenkyns, H.C., Percival, L.M.E., Hesselbo, S.P., Cartwright, J., Eldrett, J.S., Bergman, S.C., Minisini, D., 2017. Sedimentary Mercury Enrichments as a Marker for Submarine Large Igneous Province Volcanism? Evidence From the Mid-Cenomanian Event and Oceanic Anoxic Event 2 (Late Cretaceous). Geochemistry, Geophys. Geosystems. https://doi.org/10.1002/2017GC007153
Schaltegger, U., Guex, J., Bartolini, A., Schoene, B., Ovtcharova, M., 2008. Precise U-Pb

age constraints for end-Triassic mass extinction, its correlation to volcanism and Hettangian post-extinction recovery. Earth Planet. Sci. Lett. https://doi.org/10.1016/j.epsl.2007.11.031

Schaller, M.F., Wright, J.D., Kent, D.V., Olsen, P.E., 2012. Rapid emplacment of the Central Atlantic Magmatic Province as net sink for CO2. Earth Planet. Sci. Lett.

Scheingross, J. S., Repasch, M. N., Hovius, N., Sachse, D., Lupker, M., Fuchs, M., Halevy, I., Gröcke, D. R., Golombek, N. Y., Haghipour, N., Eglinton, T. I., Orfeo, O., Scleicher, A. M. 2021. The fate of fluvially-deposited organic carbon during transient floodplain storage. Earth Planet. Sci. Lett. 561: 116822.

Schoene, B., Guex, J., Bartolini, A., Schaltegger, U., Blackburn, T.J., 2010. Correlating the end-Triassic mass extinction and flood basalt volcanism at the 100 ka level. Geology. https://doi.org/10.1130/G30683.1

van de Schootbrugge, B., Bachan, A., Suan, G., Richoz, S., Payne, J. L. 2013. Microbes, mud and methane: Cause and consequence of recurrent Early Jurassic anoxia following the end-Triassic mass extinction. Palaeontology, v. 56 p. 4, p. 685–709.

Schroeder, W.H., Munthe, J., 1998. Atmospheric mercury - An overview, in: Atmospheric Environment. https://doi.org/10.1016/S1352-2310(97)00293-8

Shen, J., Algeo, T.J., Chen, J., Planavsky, N.J., Feng, Q., Yu, J., Liu, J., 2019a. Mercury in marine Ordovician/Silurian boundary sections of South China is sulfide-hosted and non-volcanic in origin. Earth Planet. Sci. Lett. https://doi.org/10.1016/j.epsl.2019.01.028

Shen, J., Chen, J., Algeo, T.J., Yuan, S., Feng, Q., Yu, J., Zhou, L., O'Connell, B., Planavsky, N.J., 2019b. Evidence for a prolonged Permian–Triassic extinction interval from global marine mercury records. Nat. Commun. https://doi.org/10.1038/s41467-019-09620-0

Shen, J., Yu, J.X., Chen, J.B., Algeo, T.X., Xu, G.Z., Feng, Q.L., Shi, X., Planavsky, N.J., Shu, W.C., Xie, S.C., 2019b. Mercury evidence of intense volcanic effects on land during the Permian-Triassic transition. Geology 47, 1117–1121.

Shen et al., 2020, Sedimentary host phases of mercury (Hg) and implications for use of Hg as a volcanic proxy, Earth and Planetary Science Letters, 543, 116333.

Si, M., McLagan, D.S., Mazot, A., Szponar, N.S., Bergquist, B.A., Lei, Y.D., Mitchell, C.P., Wania, F. 2020. Measurement of atmospheric mercury over volcanic and fumarolic regions on the North Island of New Zealand, Earth and Space Chemistry, Vol. 4 (12), DOI:10.1021/acsearthspacechem.0c00274.

Sial, A.N., Chen, J., Lacerda, L.D., Frei, R., Tewari, V.C., Pandit, M.K., Gaucher, C., Ferreira, V.P., Cirilli, S., Peralta, S., Korte, C., Barbosa, J.A., Pereira, N.S., 2016. Mercury enrichment and Hg isotopes in Cretaceous-Paleogene boundary successions: Links to volcanism and palaeoenvironmental impacts. Cretac. Res. https://doi.org/10.1016/j.cretres.2016.05.006

Sonke, J.E., 2011. A global model of mass independent mercury stable isotope fractionation. Geochim. Cosmochim. Acta 75 (16), 4577–4590.

Szponar, N., McLagan, D., Kaplan, R.J., Mitchell, C.P.J., Wania, F., Steffen, A., Stupple, G.W., Monaci, F., Bergquist, B.A., 2020. Isotopic Characterization of Atmospheric Gaseous Elemental Mercury by Passive Air Sampling, Environmental Science and Technology, 54, 17, 10533-10543.

Strasser, A., 1991. Lagoonal-peritidal sequences in carbonate environments: autocyclic and allocyclic processes, in: Einsele, G., Ricken, W., Seilacher, A. (Eds.), Cycles

and Events in Stratigraphy. Springer, Berlin, pp. 709–721.
Swift, A., 1995. A review of the nature and outcrop of the 'White Lias' facies of the Langport Member (Penarth Group: Upper Triassic) in Britain. Proc. Geol. Assoc. https://doi.org/10.1016/S0016-7878(08)80236-2
Taylor, D.G., Smith, P.L., Laws, R.A., Guex, J., 1983. The stratigraphy and biofacies trends of the Lower Mesozoic Gabbs and Sunrise formations, west-central Nevada. Can. J. Earth Sci. https://doi.org/10.1139/e83-149
Them, T.R., Jagoe, C.H., Caruthers, A.H., Gill, B.C., Grasby, S.E., Gröcke, D.R., Yin, R., Owens, J.D., 2019. Terrestrial sources as the primary delivery mechanism of mercury to the oceans across the Toarcian Oceanic Anoxic Event (Early Jurassic). Earth Planet. Sci. Lett. https://doi.org/10.1016/j.epsl.2018.11.029
Thibodeau, A.M., Bergquist, B.A., 2017. Do mercury isotopes record the signature of massive volcanism in marine sedimentary records? Geology. https://doi.org/10.1130/focus012017.1
Thibodeau, A.M., Ritterbush, K., Yager, J.A., West, A.J., Ibarra, Y., Bottjer, D.J., Berelson, W.M., Bergquist, B.A., Corsetti, F.A., 2016. Mercury anomalies and the timing of biotic recovery following the end-Triassic mass extinction. Nat. Commun. 7. https://doi.org/10.1038/ncomms11147
Todaro, S., Di Stefano, P., Zarcone, G., Randazzo, V., 2017. Facies stacking and extinctions across the Triassic–Jurassic boundary in a peritidal succession from western Sicily. Facies. https://doi.org/10.1007/s10347-017-0500-5
Todaro, S., Rigo, M., Randazzo, V., Di Stefano, P., 2018. The end-Triassic mass extinction: A new correlation between extinction events and δ13C fluctuations from a Triassic-Jurassic peritidal succession in western Sicily. Sediment. Geol. https://doi.org/10.1016/j.sedgeo.2018.03.008
Urbanek, A., 1993. Biotic crises in the history of upper silurian graptoloids: A palaeobiological model. Hist. Biol. https://doi.org/10.1080/10292389309380442
Van De Schootbrugge, B., Payne, J.L., Tomasovych, A., Pross, J., Fiebig, J., Benbrahim, M., Föllmi, K.B., Quan, T.M., 2008. Carbon cycle perturbation and stabilization in the wake of the Triassic-Jurassic boundary mass-extinction event. Geochemistry, Geophys. Geosystems. https://doi.org/10.1029/2007GC001914
Wang, X., Cawood, P.A., Zhao, H., Zhao, L., Grasby, S.E., Chen, Z.Q., Wignall, P.B., Lv, Z., Han, C., 2018. Mercury anomalies across the end Permian mass extinction in South China from shallow and deep water depositional environments. Earth Planet. Sci. Lett. https://doi.org/10.1016/j.epsl.2018.05.044
Ward, P.D., Garrison, G.H., Williford, K.H., Kring, D.A., Goodwin, D., Beattie, M.J., McRoberts, C.A., 2007. The organic carbon isotopic and paleontological record across the Triassic-Jurassic boundary at the candidate GSSP section at Ferguson Hill, Muller Canyon, Nevada, USA. Palaeogeogr. Palaeoclimatol. Palaeoecol. https://doi.org/10.1016/j.palaeo.2006.06.042
Wignall, P.B., 2001. Sedimentology of the Triassic-Jurassic boundary beds in Pinhay Bay (Devon, SW England). Proc. Geol. Assoc. https://doi.org/10.1016/S0016-7878(01)80014-6
Wotzlaw, J.F., Guex, J., Bartolini, A., Gallet, Y., Krystyn, L., McRoberts, C.A., Taylor, D., Schoene, B., Schaltegger, U., 2014. Towards accurate numerical calibration of the late triassic: Highprecision U-Pb geochronology constraints on the duration of

the Rhaetian. Geology. https://doi.org/10.1130/G35612.1
Yager, J.A., West, A.J., Corsetti, F.A., Berelson, W.M., Rollins, N.E., Rosas, S., Bottjer, D.J., 2017. Duration of and decoupling between carbon isotope excursions during the end-Triassic mass extinction and Central Atlantic Magmatic Province emplacement. Earth Planet. Sci. Lett. 473. https://doi.org/10.1016/j.epsl.2017.05.031
Zaffani, M., Jadoul, F., Rigo, M., 2018. A new Rhaetian δ 13 C org record: Carbon cycle disturbances, volcanism, End-Triassic mass Extinction (ETE). Earth-Science Rev. https://doi.org/10.1016/j.earscirev.2018.01.004
Zambardi, T., Sonke, J.E., Toutain, J.P., Sortino, F., Shinohara, H., 2009. Mercury emissions and stable isotopic compositions at Vulcano Island (Italy). Earth Planet. Sci. Lett. 277 (1), 236–243.
Zarcone, G., Petti, F.M., Cillari, A., Di Stefano, P., Guzzetta, D., Nicosia, U., 2010. A possible bridge between Adria and Africa: New palaeobiogeographic and stratigraphic constraints on the Mesozoic palaeogeography of the Central Mediterranean area. Earth-Science Rev. https://doi.org/10.1016/j.earscirev.2010.09.005
Zheng, W., Obrist, D., Weis, D., Bergquist, B.A., 2016. Mercury isotope compositions across North American forests. Glob. Biogeochem. Cycles 30 (10), 1475–1492.
Zhong Zhong, H.; Wang, W-X.. Effects of sediment composition on in- organic mercury partitioning, speciation and bioavailability in oxic surficial sediments. Environ. Poll. 2008, *151*, 222–230.
Zhou, J. Obrist, D., Dastoor, A., Jiskra, M., Ryjkov, A., 2021. Vegetation uptake of mercury and impacts on global cycling. Nature Reviews, v. 2; p. 269–284; doi: 10.1038/s43017-021-00146-y

Figure 1

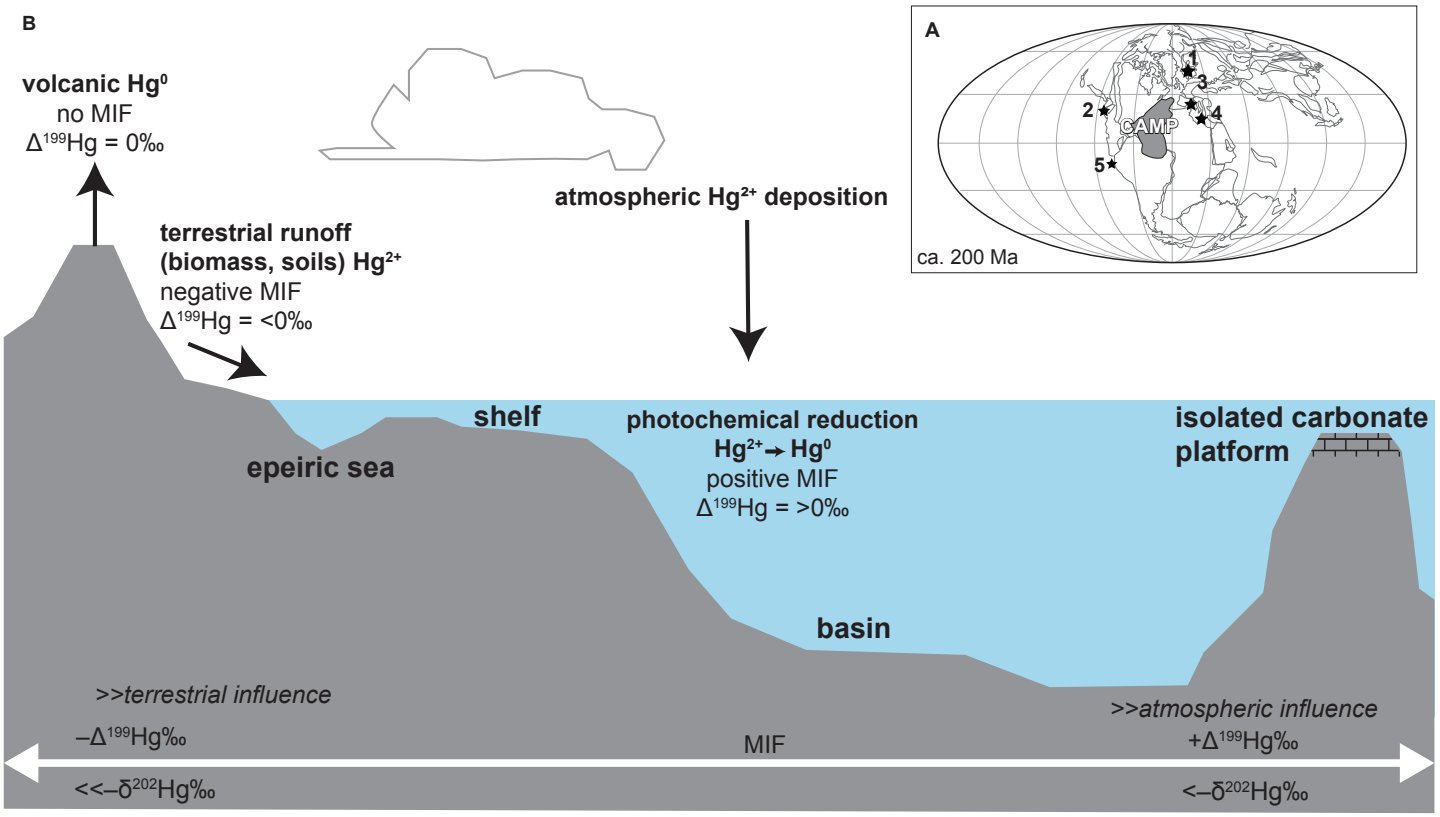
B
volcanic Hg⁰
no MIF
Δ¹⁹⁹Hg = 0‰
terrestrial runoff
(biomass, soils) Hg²⁺
negative MIF
Δ¹⁹⁹Hg = <0‰
atmospheric Hg²⁺ deposition
A
1
2
3
4
5
CAMP
ca. 200 Ma
shelf
epeiric sea
photochemical reduction
Hg²⁺ → Hg⁰
positive MIF
Δ¹⁹⁹Hg = >0‰
isolated carbonate
platform
basin
>>terrestrial influence
–Δ¹⁹⁹Hg‰
<<–δ²⁰²Hg‰
MIF
>>atmospheric influence
+Δ¹⁹⁹Hg‰
<–δ²⁰²Hg‰

FIGURE 2

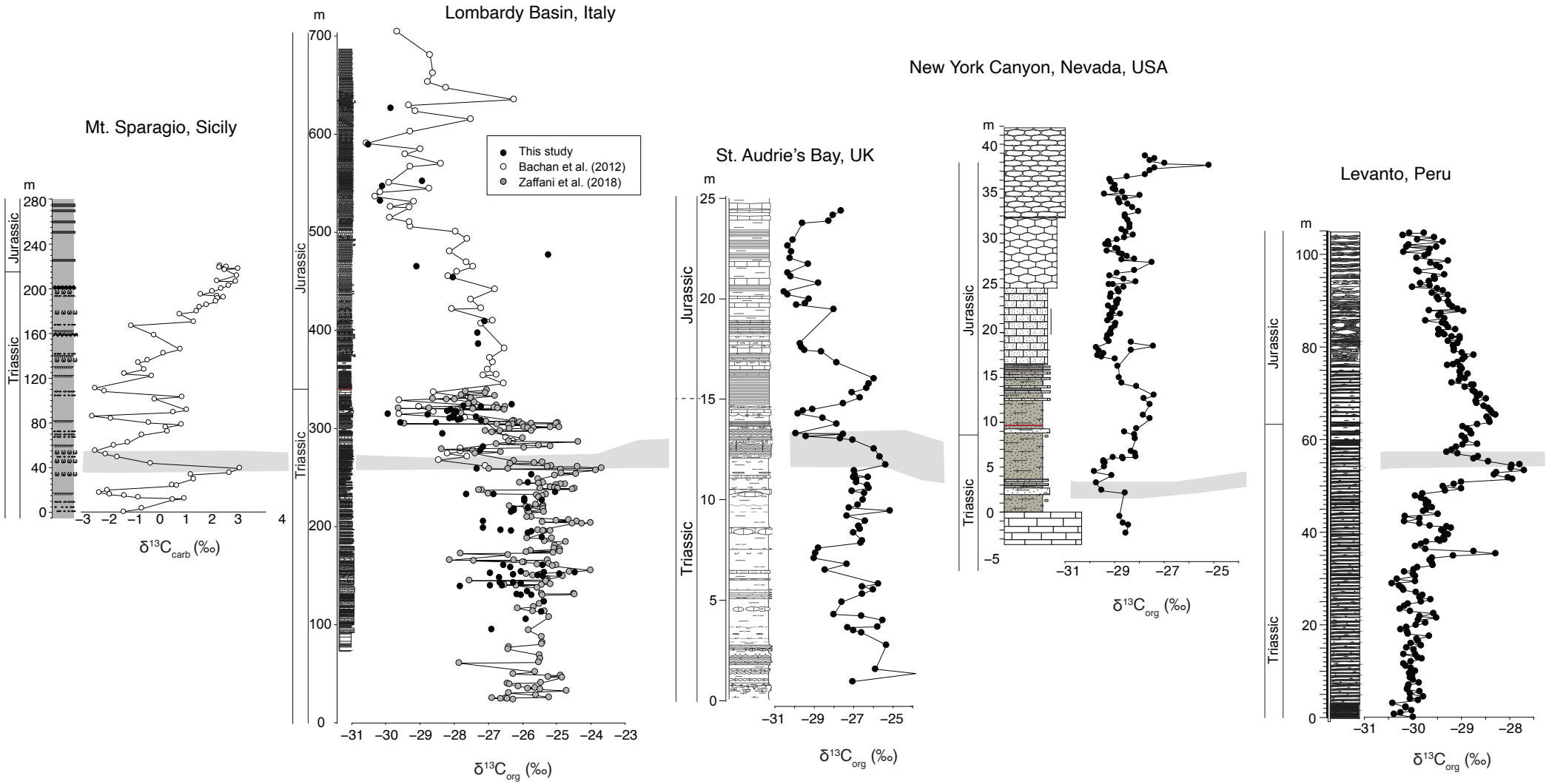
Mt. Sparagio, Sicily
m
Jurassic
Triassic
δ13Ccarb (‰)
Lombardy Basin, Italy
This study
Bachan et al. (2012)
Zaffani et al. (2018)
δ13Corg (‰)
St. Audrie's Bay, UK
δ13Corg (‰)
New York Canyon, Nevada, USA
δ13Corg (‰)
Levanto, Peru
δ13Corg (‰)

FIGURE 3

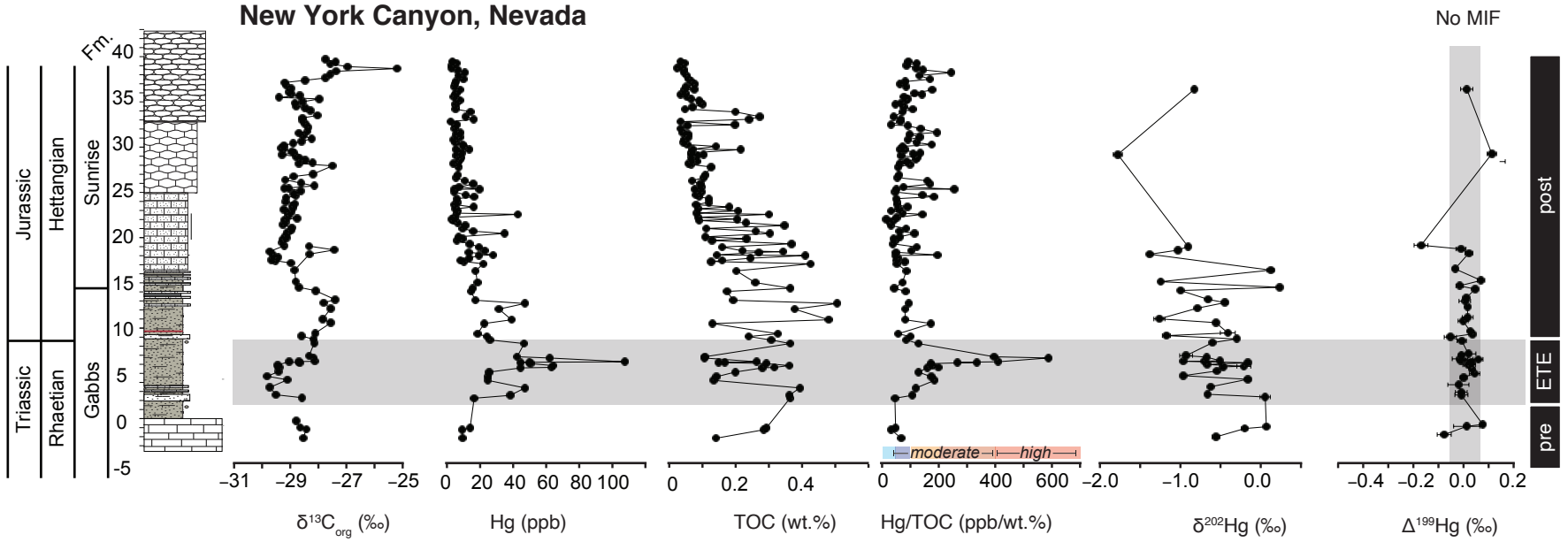

FIGURE 4

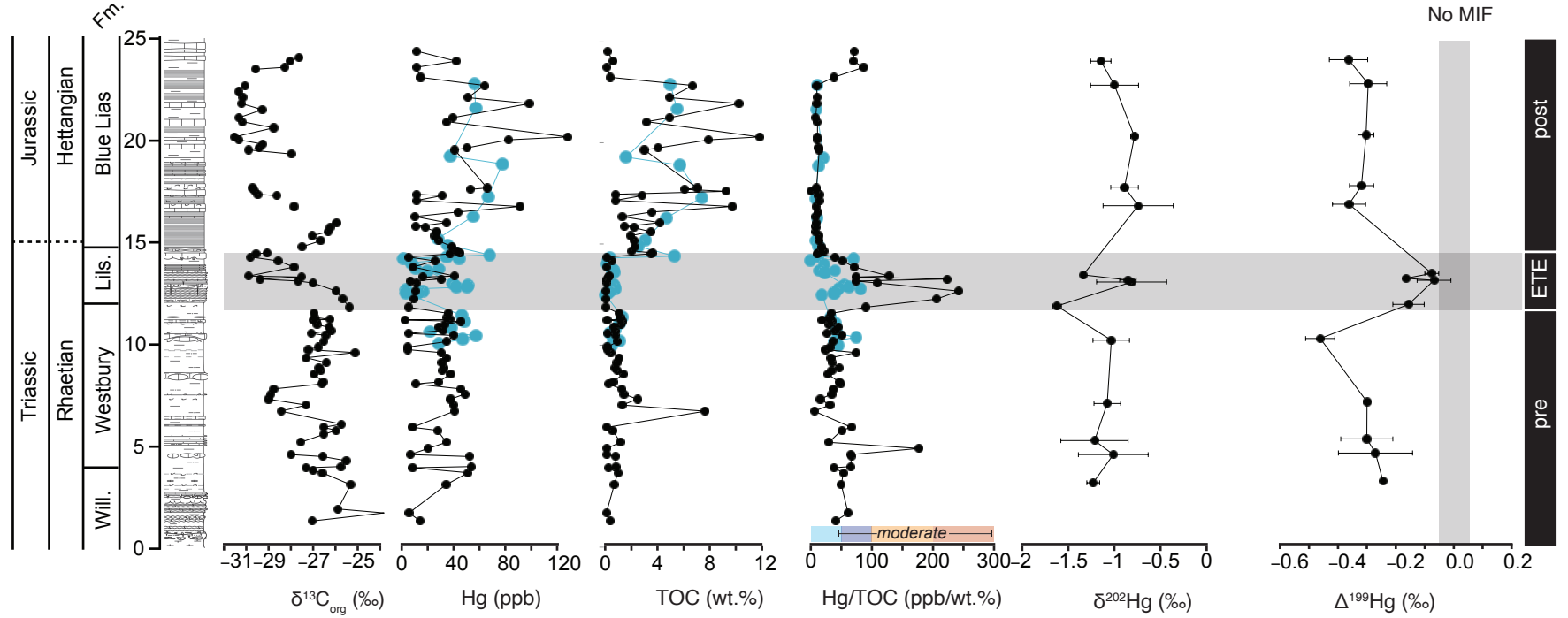

FIGURE 5

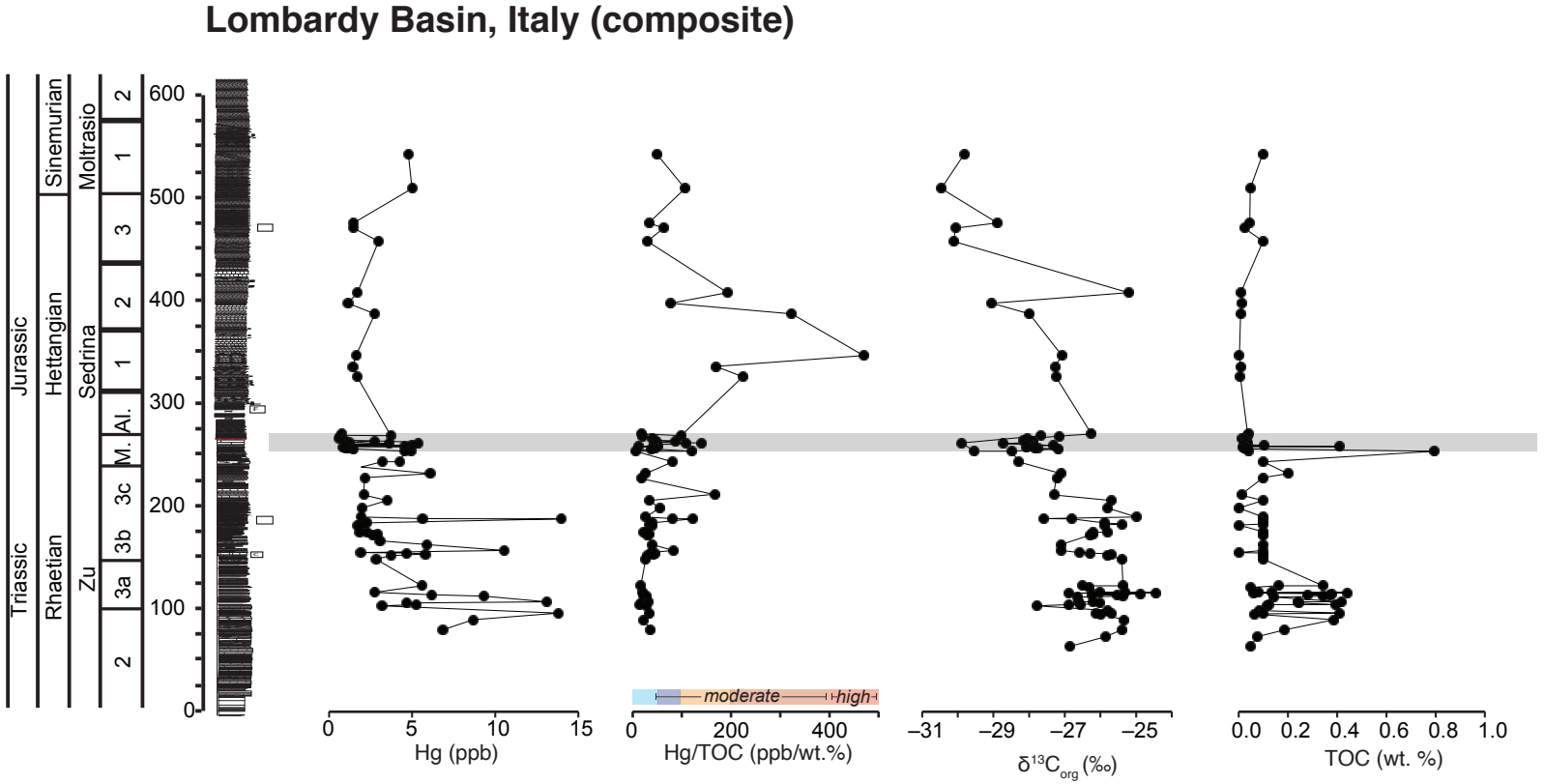

FIGURE 6

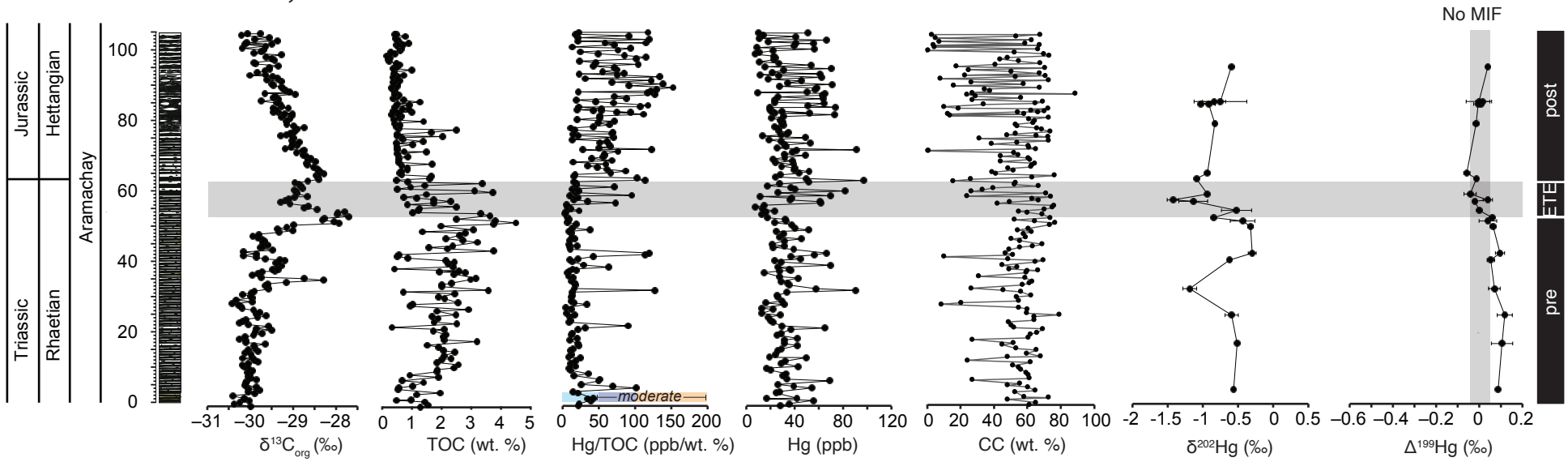

FIGURE 7

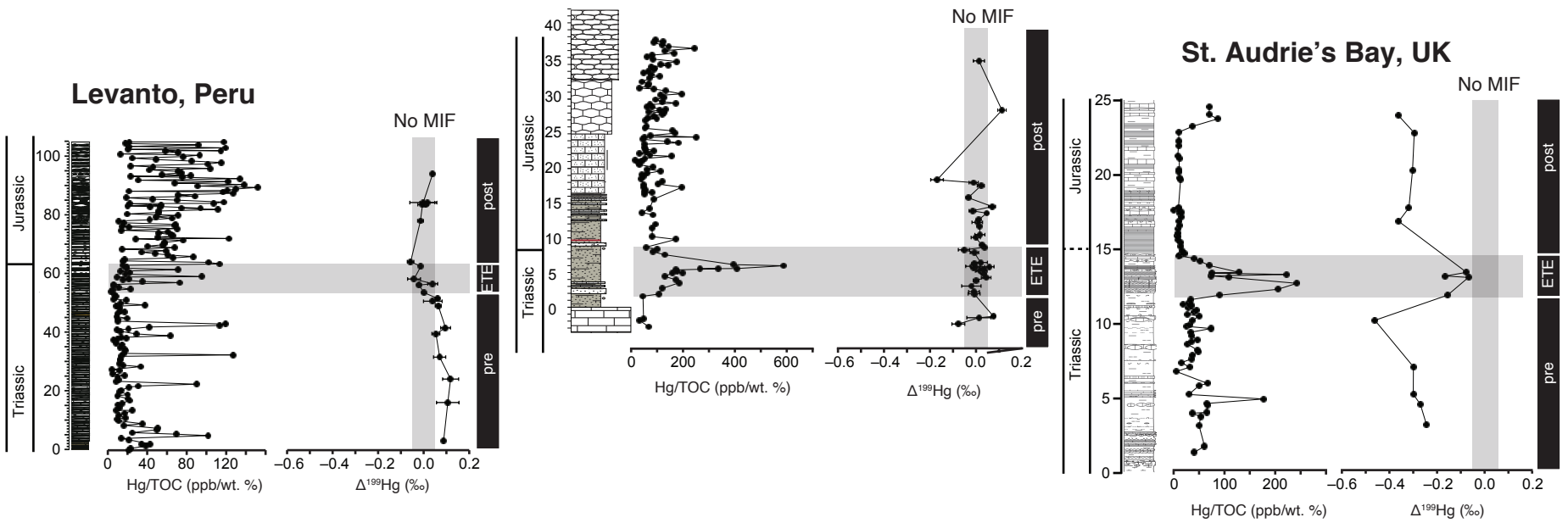
Levanto, Peru
No MIF
Jurassic
Triassic
post
ETE
pre
Hg/TOC (ppb/wt. %)
Δ199Hg (‰)
New York Canyon, Nevada
No MIF
Jurassic
Triassic
post
ETE
pre
Hg/TOC (ppb/wt. %)
Δ199Hg (‰)
St. Audrie's Bay, UK
No MIF
Jurassic
Triassic
post
ETE
pre
Hg/TOC (ppb/wt. %)
Δ199Hg (‰)

FIGURE 8

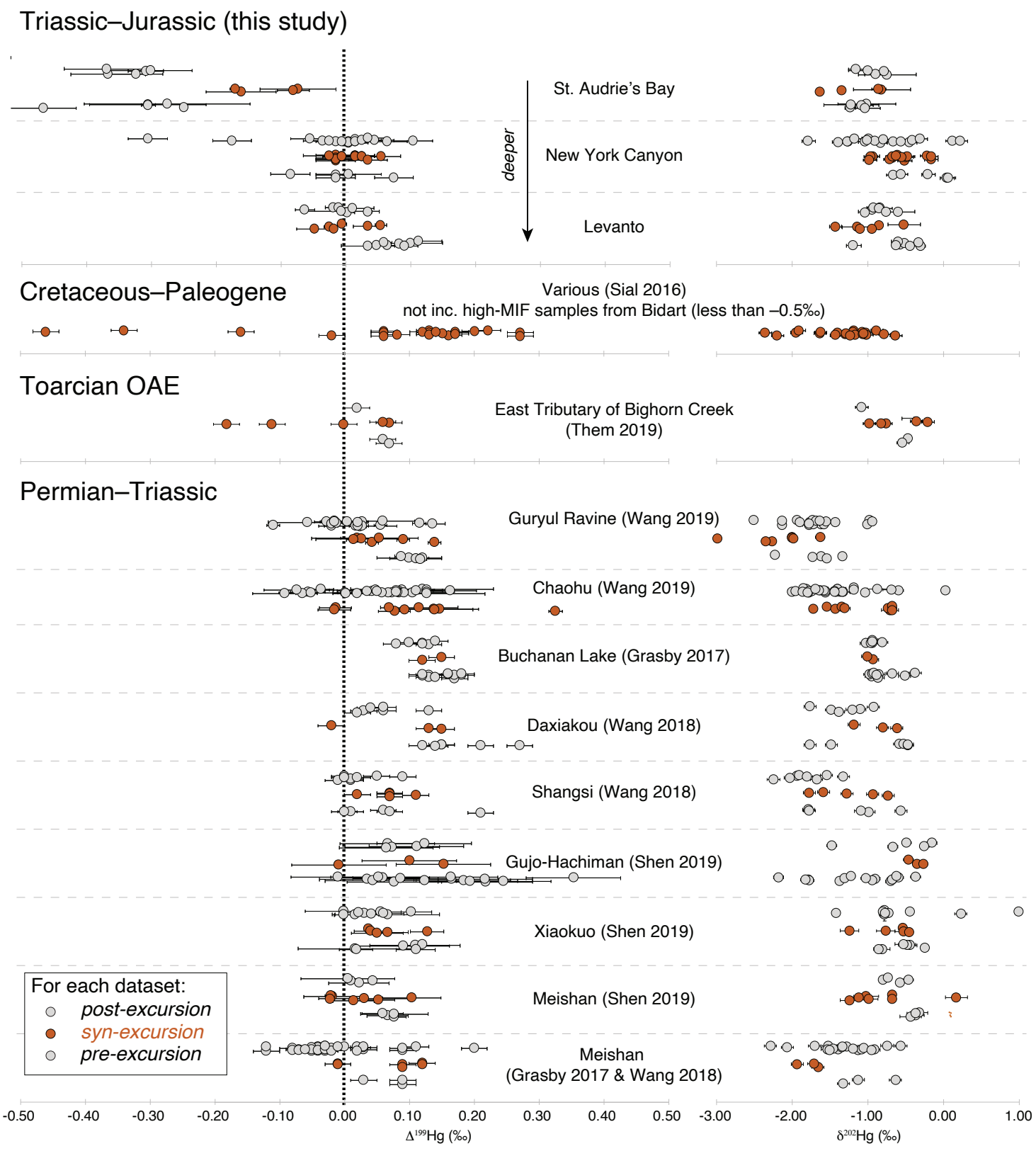
Triassic–Jurassic (this study)
St. Audrie's Bay
deeper
New York Canyon
Levanto
Cretaceous–Paleogene
Various (Sial 2016)
not inc. high-MIF samples from Bidart (less than –0.5‰)
Toarcian OAE
East Tributary of Bighorn Creek
(Them 2019)
Permian–Triassic
Guryul Ravine (Wang 2019)
Chaohu (Wang 2019)
Buchanan Lake (Grasby 2017)
Daxiakou (Wang 2018)
Shangsi (Wang 2018)
Gujo-Hachiman (Shen 2019)
Xiaokuo (Shen 2019)
Meishan (Shen 2019)
Meishan
(Grasby 2017 & Wang 2018)
For each dataset:
post-excursion
syn-excursion
pre-excursion
-0.50 -0.40 -0.30 -0.20 -0.10 0.00 0.10 0.20 0.30 0.40 0.50
Δ199Hg (‰)
-3.00 -2.00 -1.00 0.00 1.00
δ202Hg (‰)

FIGURE 9

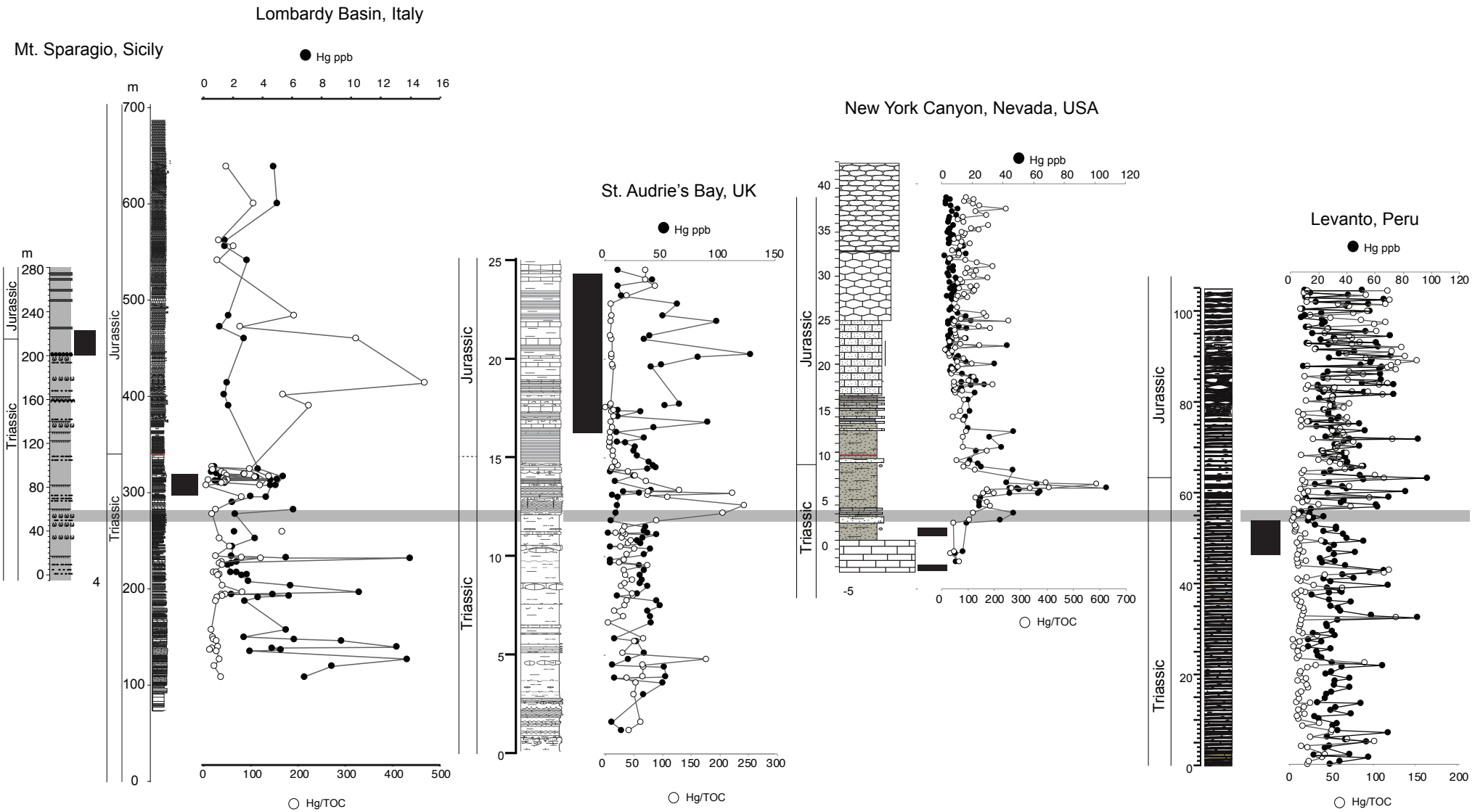
Mt. Sparagio, Sicily
Lombardy Basin, Italy
St. Audrie's Bay, UK
New York Canyon, Nevada, USA
Levanto, Peru
Hg ppb
Hg/TOC
m
Jurassic
Triassic
4

FIGURE 10

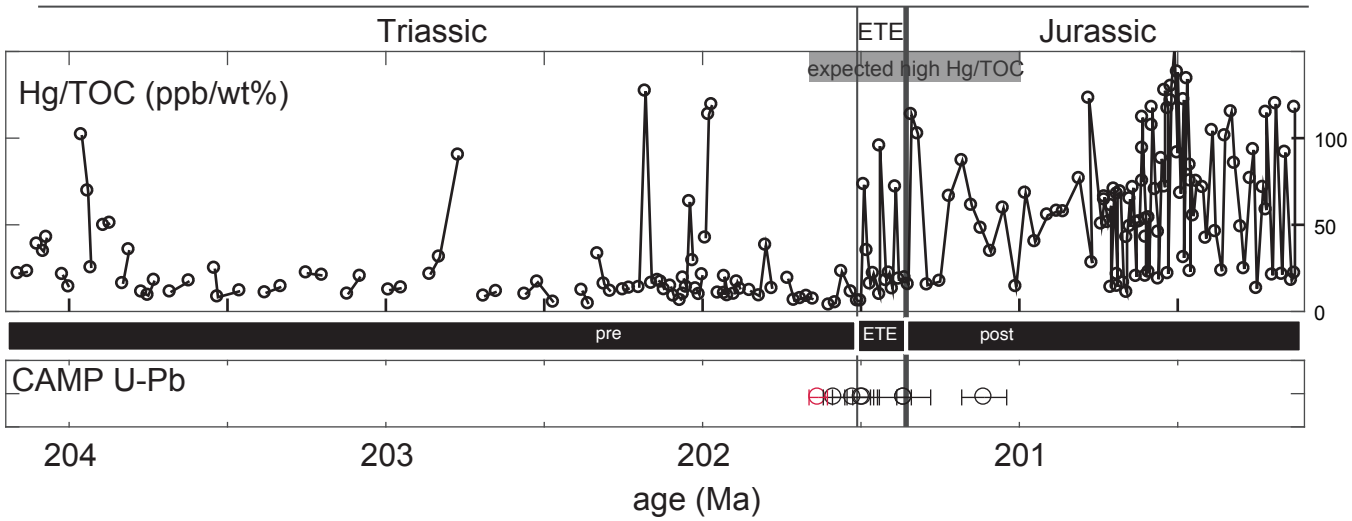
Triassic
ETE
Jurassic
expected high Hg/TOC
Hg/TOC (ppb/wt%)
100
50
0
pre
ETE
post
CAMP U-Pb
204
203
202
201
age (Ma)

FIGURE 11

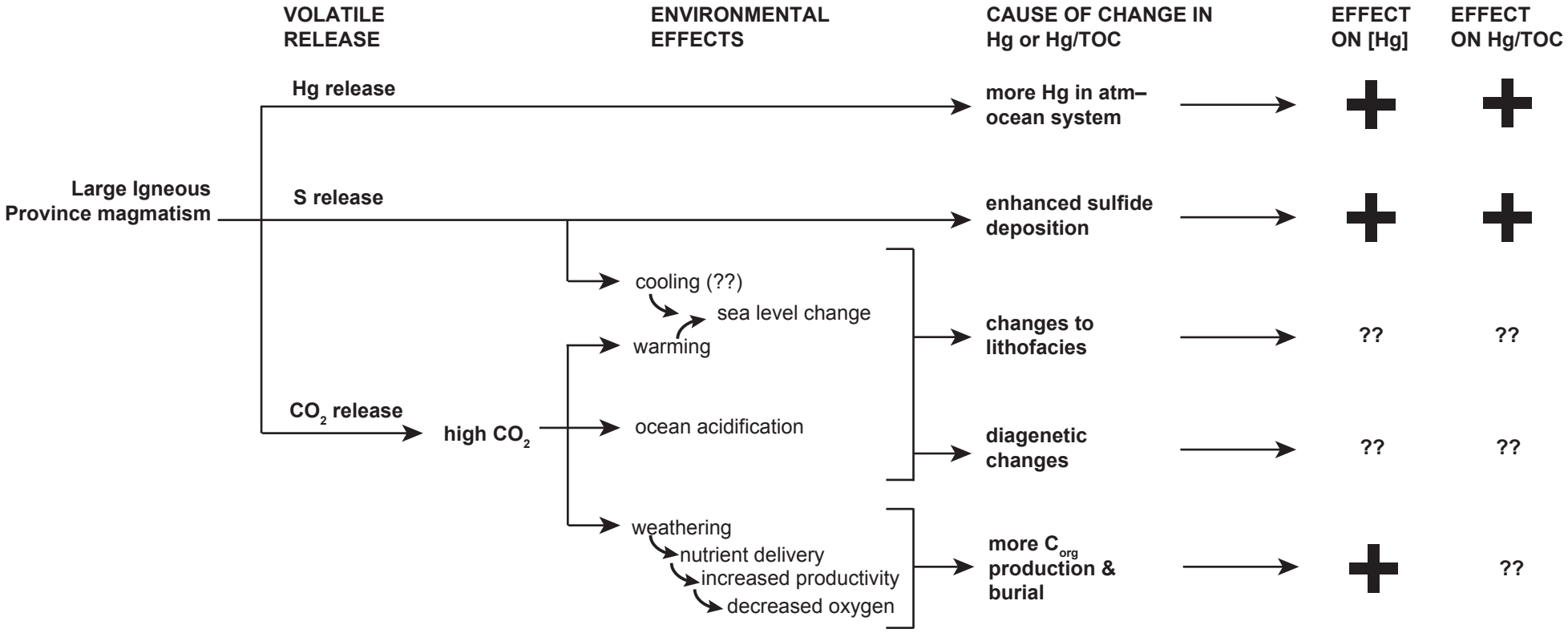
VOLATILE RELEASE
ENVIRONMENTAL EFFECTS
CAUSE OF CHANGE IN Hg or Hg/TOC
EFFECT ON [Hg]
EFFECT ON Hg/TOC
Large Igneous Province magmatism
Hg release
S release
CO2 release
high CO2
cooling (??)
sea level change
warming
ocean acidification
weathering
nutrient delivery
increased productivity
decreased oxygen
more Hg in atm–ocean system
enhanced sulfide deposition
changes to lithofacies
diagenetic changes
more Corg production & burial
??
??
??
??
??